



HAL
open science

O3 variability in the troposphere as observed by IASI over 2008-2016: Contribution of atmospheric chemistry and dynamics

Catherine Wespes, Daniel Hurtmans, Cathy Clerbaux, Pierre-François Coheur

► **To cite this version:**

Catherine Wespes, Daniel Hurtmans, Cathy Clerbaux, Pierre-François Coheur. O3 variability in the troposphere as observed by IASI over 2008-2016: Contribution of atmospheric chemistry and dynamics. *Journal of Geophysical Research: Atmospheres*, 2017, 122 (4), pp.2429-2451. 10.1002/2016JD025875 . insu-01451930

HAL Id: insu-01451930

<https://insu.hal.science/insu-01451930>

Submitted on 6 Sep 2020

HAL is a multi-disciplinary open access archive for the deposit and dissemination of scientific research documents, whether they are published or not. The documents may come from teaching and research institutions in France or abroad, or from public or private research centers.

L'archive ouverte pluridisciplinaire **HAL**, est destinée au dépôt et à la diffusion de documents scientifiques de niveau recherche, publiés ou non, émanant des établissements d'enseignement et de recherche français ou étrangers, des laboratoires publics ou privés.

RESEARCH ARTICLE

10.1002/2016JD025875

Key Points:

- Global assessment of the geophysical mechanisms behind the tropospheric O₃ variability using 8 years of IASI satellite data
- Global patterns of the main O₃ drivers (including NAO, QBO, and ENSO) are provided
- Identification of a significant 4-month time-lag in the response of O₃ to ENSO into the middle and high latitudes

Correspondence to:

C. Wespes,
cwespes@ulb.ac.be

Citation:

Wespes, C., D. Hurtmans, C. Clerbaux, and P.-F. Coheur (2017), O₃ variability in the troposphere as observed by IASI over 2008–2016: Contribution of atmospheric chemistry and dynamics, *J. Geophys. Res. Atmos.*, 122, 2429–2451, doi:10.1002/2016JD025875.

Received 31 AUG 2016

Accepted 27 JAN 2017

Accepted article online 1 FEB 2017

Published online 20 FEB 2017

O₃ variability in the troposphere as observed by IASI over 2008–2016: Contribution of atmospheric chemistry and dynamics

C. Wespes¹ , D. Hurtmans¹, C. Clerbaux^{1,2} , and P.-F. Coheur¹

¹Spectroscopie de l'Atmosphère, Service de Chimie Quantique et Photophysique, Faculté des Sciences, Université Libre de Bruxelles (U.L.B.), Brussels, Belgium, ²Sorbonne Universités, UPMC Université Paris 06, Université Versailles St-Quentin, CNRS/INSU, LATMOS-IPSL, Paris, France

Abstract We analyze the ozone (O₃) variability in the troposphere (from ground to 300 hPa) using 8 years (January 2008 to March 2016) of O₃ profile measurements provided by the Infrared Atmospheric Sounding Interferometer (IASI) on board the MetOp satellite. The capability of IASI to monitor the year-to-year variability in that layer is examined first in terms of vertical sensitivity, a priori contribution, and correlations in the deseasonalized anomalies with the upper layers. We present global patterns of the main geophysical drivers (e.g., solar flux, Quasi-biennial Oscillation—QBO, North Atlantic Oscillation—NAO, and El Niño–Southern Oscillation—ENSO) of IASI O₃ variations, obtained by applying appropriate annual and seasonal multivariate regression models on time series of spatially gridded averaged O₃. The results show that the models are able to explain most of the O₃ variability captured by IASI. Large O₃ changes in the North Arctic/Euro-Atlantic sector and over the equatorial band are attributed to the NAO and the QBO effects, respectively. ENSO is modeled as the main contributor to the O₃ variations in the tropical band where direct effects of warm and cool ENSO phases are highlighted with a clear tropical-extratropical gradient. A strong west-east gradient in the tropics is also found and likely reflects an indirect effect related to ENSO dry conditions. Finally, we also show that the ENSO perturbs the O₃ variability far from the tropics into middle and high latitudes where a significant 4-month time-lag in the response of O₃ to ENSO is identified for the first time.

1. Introduction

Monitoring tropospheric ozone (O₃) and its time evolution is needed to understand the present climate and apprehend future climate changes. O₃ is a key trace gas in the troposphere, being formed from reactions involving carbon monoxide (CO), volatile organic compounds (VOCs), and nitrogen oxides (NO_x); and it plays a major role in air quality, having dangerous effects on human health and ecosystems. It is also a significant greenhouse gas, which contributes to the radiative forcing of the atmosphere, being a strong greenhouse gas where in addition, due to its long lifetime relatively to transport timescales [Fusco and Logan, 2003], O₃ is a good candidate for intercontinental transport on hemispheric scales, affecting regional air quality away from source regions in downwind receptor regions [e.g., Stohl et al., 2002; Hudman et al., 2004; Parrish et al., 2012, and references therein].

The two main sources of tropospheric O₃ are the in situ photochemical production and the downward transport of O₃ produced in the stratosphere by the large-scale Brewer-Dobson circulation. While changes in tropospheric O₃ since the latter half of the twentieth century are largely attributed to increasing anthropogenic emissions and fueled photochemical O₃ production [e.g., Wang and Jacob, 1998; Oltmans et al., 2006; Intergovernmental Panel on Climate Change, 2007; Vestreng et al., 2009], recent studies have shown that they are also significantly influenced by those in stratospheric ozone through specific dynamical processes. These studies reported strong vertical correlations between lower stratospheric and tropospheric ozone on local and regional scales [e.g., Tarasick et al., 2005; Thouret et al., 2006; Terao et al., 2008; Hess and Zbinden, 2013]. Other factors such as CH₄, CO amount, and solar ultraviolet radiation may also influence tropospheric O₃, as well as changes in air mass circulation associated with large-scaled dynamical modes such as the North Atlantic and the El Niño–Southern Oscillation. These later contribute to large interannual and decadal variations at a regional scale and influence the strength of the polar vortex and the stratosphere/troposphere exchanges (STE) [e.g., Thouret et al., 2006; Ziemke and Chandra, 2003; Zeng and Pyle, 2005; Chandra et al., 1998, 2002, 2007; Koumoutsaris et al., 2008; Voulgarakis et al., 2011; Pausata et al., 2012; Ziemke et al., 2015, and references therein].

As a consequence, considering trends in anthropogenic emissions only does not suffice to qualitatively explain the interannual variability and trend in tropospheric ozone [Fiore *et al.*, 2009; Cooper *et al.*, 2010; Logan *et al.*, 2012; Wilson *et al.*, 2012]. Because of complex combination/interaction of (photo-)chemistry and dynamics, their origins are still challenging to attribute and to understand. This results in large contradictions in trend determined from independent studies and data sets in the troposphere [e.g., Logan, 1999; Oltmans *et al.*, 2006; Fusco and Logan, 2003; Tarasick *et al.*, 2005; Zbinden *et al.*, 2006; Thouret *et al.*, 2006; Fiore *et al.*, 2009; Logan *et al.*, 2012]. In order to improve on this understanding, it is of particular importance to accurately and simultaneously quantify the origins of the interannual variability in tropospheric O₃, as it has already been achieved for stratospheric and total O₃ columns by using multivariate regression approaches [e.g., Mäder *et al.*, 2007; Frossard *et al.*, 2013; Rieder *et al.*, 2013; Knibbe *et al.*, 2014]. Such methods aim to gain a better understanding of the chemical and dynamical mechanisms behind the interannual variability and, therefore, to allow accurate examination of the trends observed in tropospheric column ozone. To the best of our knowledge, regression methods have only been applied on regional and global observations of tropospheric O₃ in a few recent studies [Oman *et al.*, 2013; Heue *et al.*, 2016; Ebojje *et al.*, 2016; Olsen *et al.*, 2016], which underlines the lack of comprehensive and continuous global observations over a long period in the troposphere.

The new generation of nadir-looking instruments onboard polar-orbiting satellites (e.g., Infrared Atmospheric Sounding Interferometer (IASI), Global Ozone Monitoring Experiment (GOME)-2, Tropospheric Emission Spectrometer (TES), and Ozone Monitoring Instrument (OMI)) provides accurate measurements to monitor the production and transport of tropospheric O₃ at a global scale for about one decade, despite the geometry of these sounders which makes difficult to detect the small part of the atmospheric O₃ in the troposphere. Recent studies have, in particular, demonstrated that the IASI (Infrared Atmospheric Sounding Interferometer) sounders aboard the European MetOp platforms, which are operational since October 2006, allow measuring global distributions and time evolution of tropospheric O₃, and even air pollution episodes [e.g., Eremenko *et al.*, 2008; Dufour *et al.*, 2010; Safieddine *et al.*, 2013; Wespes *et al.*, 2016].

Here we use the 8 first years (January 2008 to March 2016) of the O₃ data set available from IASI onboard MetOp-A to provide geographical patterns of regression coefficients for seasonal and non-seasonal O₃ dependencies in the troposphere. This approach is built on previous analysis of the first 6 year time series of IASI O₃ total columns and of several partial columns covering both the troposphere and the stratosphere on 20° zonal bands which is reported in Wespes *et al.* [2016]. We further analyze and interpret the O₃ variations in the troposphere at a global scale with a series of explanatory variables implemented in a multivariate regression model. In section 2, we briefly review IASI and the retrieved tropospheric O₃ columns. We also describe the multivariate regression model which has been specifically developed for fitting O₃ time series in the troposphere. In section 3, we evaluate the performance of the regression model (annual and seasonal) in terms of residual errors, of IASI variations explained by the model, and of Pearson's goodness of fit statistic. In section 4, by exploiting both the annual and the seasonal formulations of the regression model, we analyze the role of the main O₃ drivers on the temporal and spatial variations observed by IASI between 2008 and 2016. We particularly focus on the influence of El Niño/Southern Oscillation (ENSO).

2. IASI Measurements and Statistical Model

2.1. O₃ Measurements and Retrieval Method

The IASI instrument on board the MetOp-A platform was launched in October 2006 in a Sun-synchronous orbit. It is a Fourier transform spectrometer that measures the thermal infrared emission of the Earth-atmosphere system between 645 and 2760 cm⁻¹. With measurements taken every 50 km along the track of the satellite at nadir and over a swath of 2200 km across track, IASI provides global coverage of the Earth twice a day (at 9:30 and 21:30 mean local solar time) with a set of four simultaneous footprints of 12 km at nadir. The spectrometer is characterized by a good spectral resolution and a low radiometric noise, which allows the retrieval of numerous gas-phase species in the troposphere [e.g., Clerbaux *et al.*, 2009; Hilton *et al.*, 2012; Clarisse *et al.*, 2011, and references therein].

O₃ profiles are retrieved with the FORLI-O₃ (Fast Operational/Optimal Retrievals on Layers for IASI) processing chain set up by the ULB and LATMOS groups (see Hurtmans *et al.* [2012] for a description of the retrieval

parameters and performances) which relies on a fast radiative transfer and retrieval methodology based on the optimal estimation method [Rodgers, 2000]. In the version used in this study (FORLI-O₃ v20140922), it provides O₃ profiles on a uniform 1 km vertical grid on 40 layers from surface up to 40 km. The a priori profile and the a priori covariance matrix are built from the Logan/Labow/McPeters climatology [McPeters et al., 2007], and only one single globally uniform O₃ a priori profile and variance-covariance matrix are used [Hurtmans et al., 2012]. The FORLI-O₃ profiles and partial columns have undergone a series of validation using available ground-based, aircraft, O₃ sonde and other satellite observations over local areas and/or selected time periods [Anton et al., 2011; Dufour et al., 2012; Gazeaux et al., 2012; Parrington et al., 2012; Pommier et al., 2012; Scannell et al., 2012; Oetjen et al., 2014]. Recently, several years of FORLI-O₃ v20140922 products have been validated on the global scale against a series of independent observations (GOME-2, Dobson, Brewer, SAOZ (Système d'Analyse par Observation Zénithale), and ozonesondes data) during the period 2008–2014 [Boynard et al., 2016]. The studies show good agreements between the IASI data and independent measurements, but they reported a small but consistent systematic positive bias for the overall vertical profile (bias <10% on average).

As in Wespes et al. [2016], only daytime O₃ measurements (defined with a solar zenith angle to the Sun < 80°) characterized by a good spectral fit (e.g., based on quality flags rejecting biased or sloped residuals, suspect averaging kernels, maximum number of iteration exceeded, ...) have been analyzed in this study. They are characterized by a better vertical sensitivity to the troposphere associated with a higher surface temperature and a higher thermal contrast [e.g., Clerbaux et al., 2009]. Cloud-contaminated IASI scenes characterized by a fractional cloud cover below 13% are also filtered out using cloud information from the Eumetcast operational processing system [August et al., 2012].

Figure 1 illustrates, for the year 2014, the seasonal distributions of averaged FORLI-O₃ columns from the surface to 300 hPa (called MLT—middle-low troposphere—in this study; Figure 1a) of the associated degree of freedom for signal (DOFS) (Figure 1b) and of the a priori contribution to the MLT columns due to the limited vertical sensitivity of the IASI instrument (calculated as $x_a \cdot \mathbf{A}(x_a)$, where x_a is the a priori profile and \mathbf{A} the averaging kernel matrix, following the formalism of Rodgers [2000]) (Figure 1c). Based on previous sensitivity analyses [Wespes et al., 2012, 2016], the tropospheric layer is here defined as ranging from ground to 300 hPa to limit as much as possible the influences of the stratospheric O₃ and to include the altitude of maximum sensitivity of IASI in the troposphere (around 4–8 km altitude for most of the situations). The large O₃ columns observed in the northern latitudes during winter-spring (>30 DU) suggest, however, a strong stratospheric influence related to the medium vertical sensitivity of IASI in lower layers in these latitudes as shown by the lowest values for DOFS (Figure 1b), to tropopause height variations, or to STE processes. The contribution of the stratosphere into the MLT O₃ variations as seen by IASI has been previously estimated in Wespes et al. [2016, supporting information] with a global 3-D chemical transport model (MOZART-4) to amount between 30% and 65% depending on the region and the season. The largest contribution from the stratosphere is found in regions north of 70°N in April, while the northern midlatitudes in spring-summer show the smallest stratospheric contribution, i.e., the O₃ variations are mainly originating from the troposphere: they are characterized by the largest sensitivity (DOFS ~0.8) over the continental regions and usually by weak episodes of stratosphere-troposphere exchange. The natural tropospheric contribution to the IASI-observed MLT signal (obtained by subtracting from the IASI MLT O₃ time series, the a priori contribution, the artificial stratospheric one due to the IASI limited sensitivity, and the natural portion coming from the stratosphere) was previously calculated as reaching ~60% in the 30°N–70°N latitude band [see Wespes et al., 2016, supporting information]. The high O₃ records that we observe recurrently from year to year over the highly populated areas of China and of northern India in summer are likely due to the photochemical production of O₃ from anthropogenic precursor emissions [e.g., Logan, 1985; Fusco and Logan, 2003; Dufour et al., 2010; Cooper et al., 2010; Wilson et al., 2012; Safieddine et al., 2013; Wespes et al., 2016], while those observed over the eastern part of the Mediterranean Basin during summer have been assigned to STE processes [e.g., Safieddine et al., 2014]. The seasonal distributions also reflect the large fire activity in spring around 20°S–40°S. Finally, we find in almost all situations that the a priori contributions do not exceed 20% and are lower than 10% in the northern midlatitudes in spring-summer where the IASI sensitivity is the highest. This a priori contribution is also, as expected, found to be partly correlated with the DOFS.

To better describe the origin of the O₃ variability observed by IASI in the MLT and to better evaluate the impact of the upper layers into the small MLT variations, we perform the deseasonalization of the IASI O₃ time series by removing the climatological monthly means over the IASI period. The deseasonalized O₃ anomalies

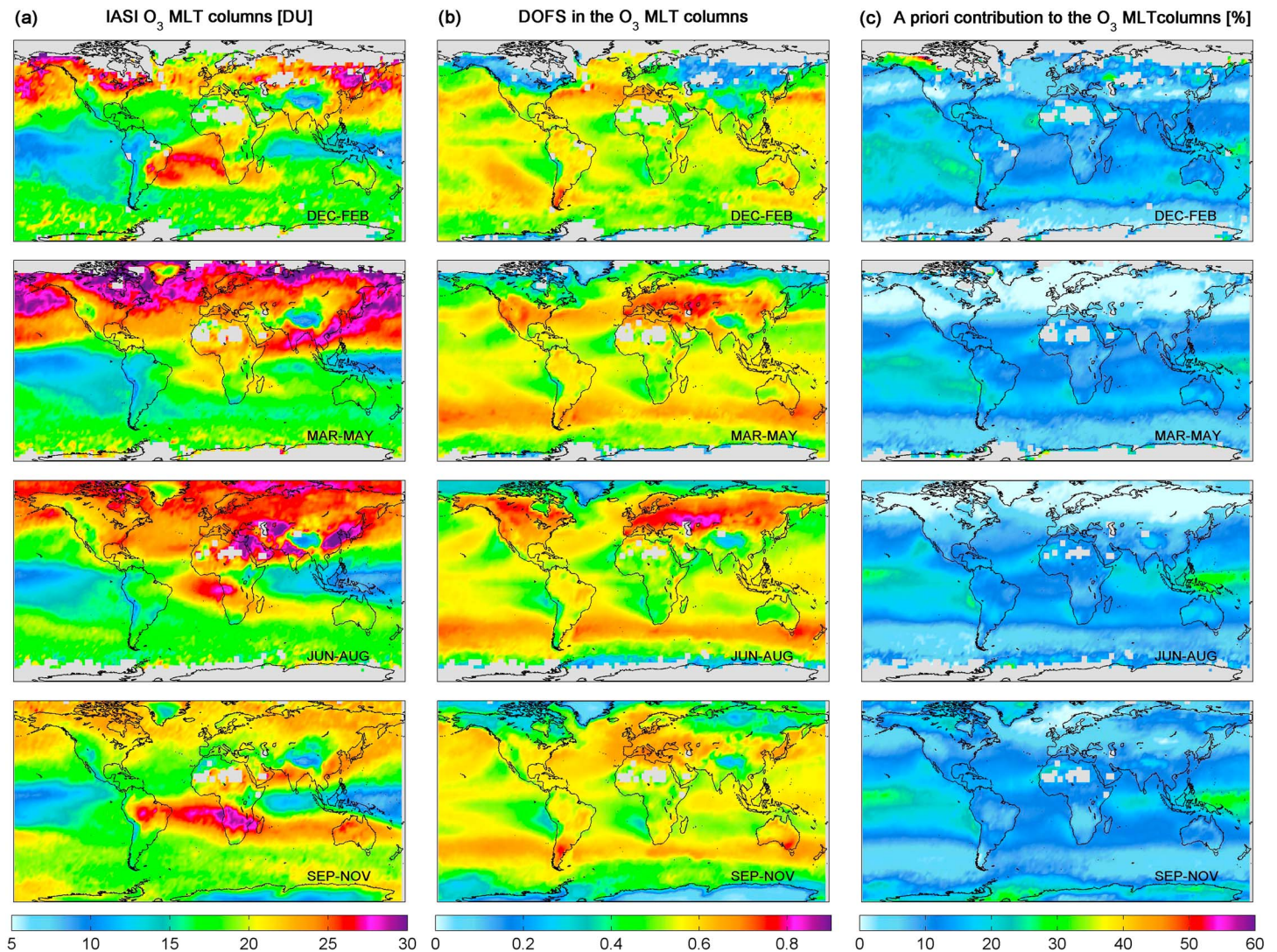


Figure 1. Seasonal distributions for the year 2014 of (a) O₃ in the ground to 300 hPa columns (MLT), (b) DOFS, and (c) a priori contributions (given in percent), averaged over a 2.5° × 2.5° grid box.

are calculated as $[100 \times (O_{3\text{Month}} - O_{3\text{Month}}^{\text{Clim}}) / O_{3\text{Month}}^{\text{Clim}}]$, where $O_{3\text{Month}}$ are the monthly means of the O₃ columns in the various layers and $O_{3\text{Month}}^{\text{Clim}}$ are the climatological means calculated independently for each month by averaging over the period of the IASI observations [e.g., Jones et al., 2009; Randel and Thompson, 2011]. This methodology removes effects of the a priori contribution and geophysical processes that are recurrent from year to year and, therefore, highlights any small perturbations in the observed seasonal cycles. The global distribution of the annual deseasonalized O₃ anomalies averaged over 2008–2016 and over 2.5° × 2.5° grid boxes in four different atmospheric layers defined (identically to Wespes et al. [2016]) as follows: the upper stratosphere (25–3 hPa; UST panel), the middle-low stratosphere (150–25 hPa; MLST panel), the upper troposphere-lower stratosphere (300–150 hPa; UTLS panel), and the MLT (MLT panel) are illustrated in Figure 2a (in percent). Figure 2b represents the correlation coefficients between the time series of deseasonalized O₃ anomalies measured in the MLT and the upper layers, referred as $R_{\text{MLT-UTLS}}$, $R_{\text{MLT-MLST}}$, and $R_{\text{MLT-UST}}$. The deseasonalization removes from the correlation maps the effects of the seasonal variations induced by the Brewer-Dobson circulation and the solar insolation which are the main drivers of the O₃ variability and which influence the variations in both tropospheric and stratospheric O₃ [Wespes et al., 2016]. The deseasonalized anomaly map for the MLT (Figure 2a, fourth panel) exhibits very different patterns compared to the upper layers. While the QBO effect is likely seen in the equatorial

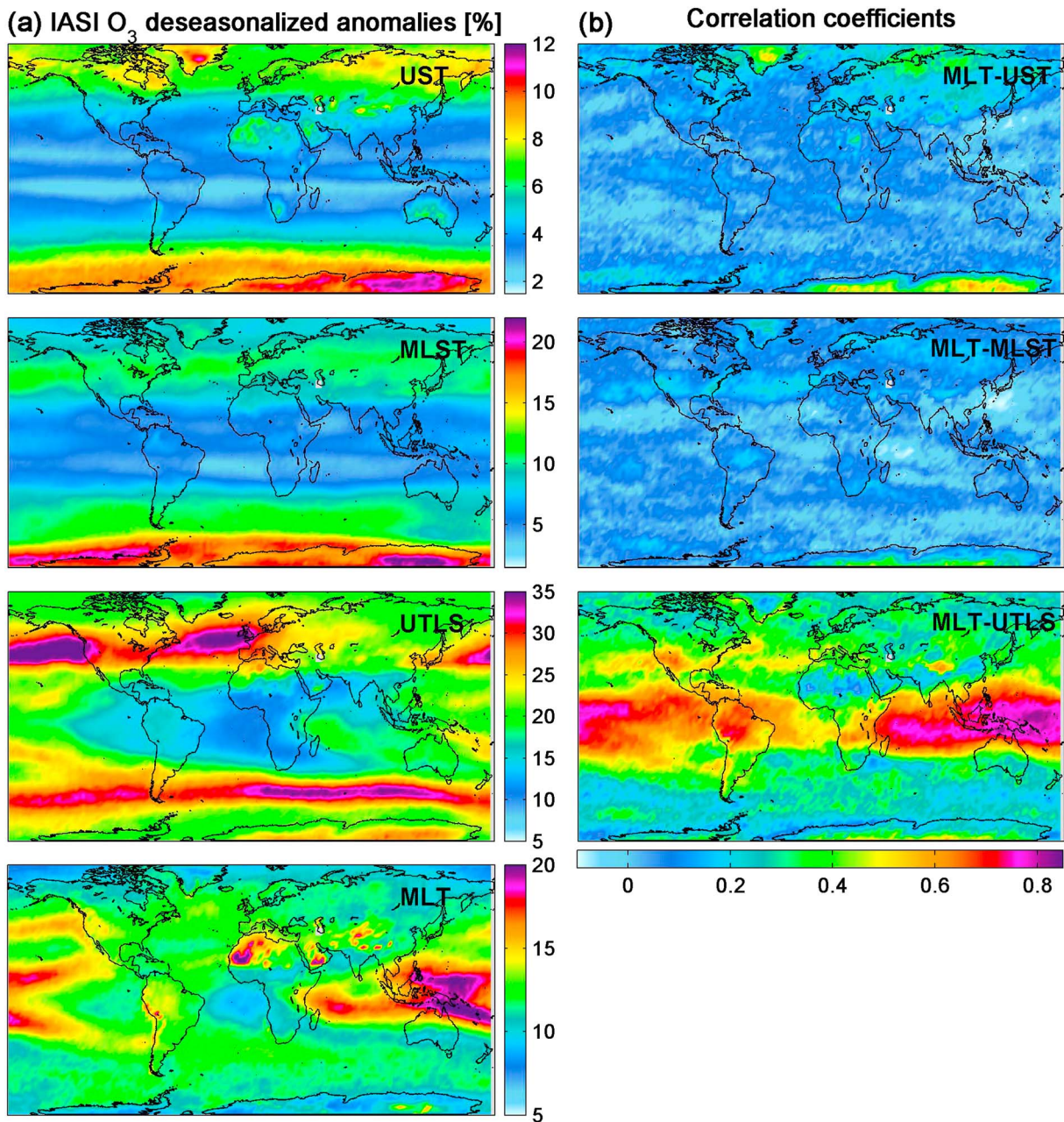


Figure 2. Global distribution of (a) the IASI O₃ deseasonalized anomalies (in percent) for the MLT (ground to 300 hPa), UTLS (300–150 hPa), MLST (150–25 hPa), and UST (above 25 hPa) layers and (b) the correlation coefficients between the daily O₃ deseasonalized anomalies in the MLT and in the upper layers, averaged over 2008–2016 and over a 2.5° × 2.5° grid box.

region and the polar O₃ dominates the anomalies in the MLST and in the UST (see Figure 2a, UST and MLST panels), the MLT presents the highest anomalies in the western tropical Pacific where it reaches ~25% and a strong decrease over the eastern Pacific (see Figure 2a, MLT panel). This region is well known to be significantly affected by the ENSO, which is one of the most important dynamic for the climate variability on interannual timescales and which varies strongly from year to year [e.g., Randel *et al.*, 2011; Ziemke *et al.*, 2010]. The effect of this dynamical process on the O₃ levels will be estimated in section 4. We also note high anomalies above the desert regions, mainly in North Africa and Saudi Arabia. This is likely related to remaining poor spectral fits above surfaces characterized by sharp emissivity variations at 10 μm, typically above desert sand [Hurtmans *et al.*, 2012]. The capability of IASI to distinguish the dynamical and chemical processes occurring in the troposphere is verified by the low correlations between the MLT and the upper

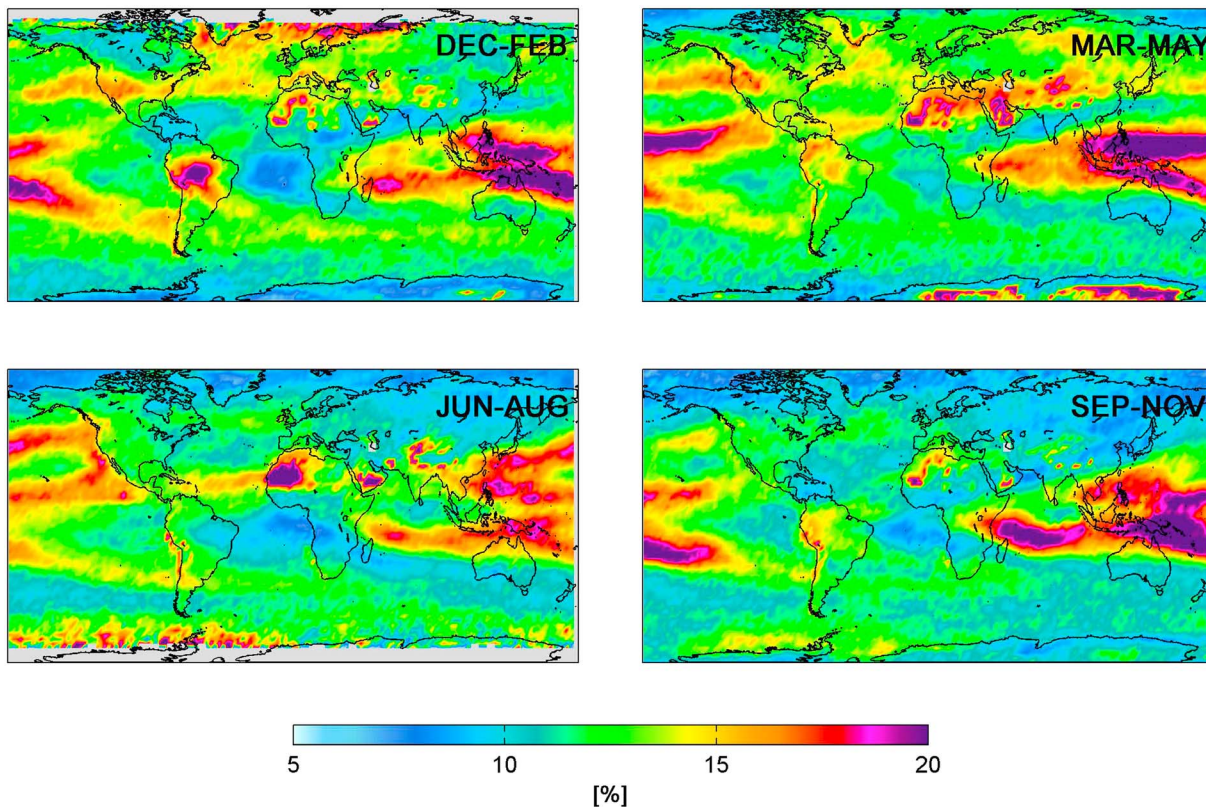


Figure 3. Seasonal distributions of the IASI O₃ deseasonalized anomalies (in percent) for the MLT (ground to 300 hPa) averaged over January 2008 to March 2016 and over a 2.5° × 2.5° grid box.

layers (R_{MLT_MLST} and $R_{MLT_UST} < 0.3$ on average), with exceptions in regions characterized by low sensitivity—typically over cold polar regions (R_{MLT_MLST} and $R_{MLT_UST} > 0.5$). On the contrary, we find high positive correlations between the MLT and the UTLS. That layer is characterized by the lower vertical sensitivity of IASI [Wespes *et al.*, 2016] which, hence, explains the resemblances of the anomalies in the UTLS to those found in the MLT and also in the upper layers. Furthermore, the QBO and ENSO are important components of the dynamic in both the troposphere and the lower stratosphere, likely explaining the highest MLT-UTLS correlations found in the tropics. The anomalies in the UTLS also reflect large variations in the tropopause height around the polar vortex edge in the both hemispheres. The deseasonalized anomalies for the MLT are further illustrated in Figure 3 for the seasonal averages. The likely effect of the ENSO phenomenon is clearly visible throughout the year but in particular during the periods from December to February and from March to May. Another interesting feature is the detection of high anomalies downwind China across the northern Pacific and reaching the West Coast of U.S. mainly during the June–August period, which is probably reflecting the transport of photochemically produced anthropogenic O₃.

2.2. Multivariate Regression Models and Fitting Procedure

To unambiguously attribute the factors responsible for the O₃ variability, we use, similar to what was done in Wespes *et al.* [2016], a multiple linear regression model accounting for a linear trend, for variations related to dynamical processes (QBO, ENSO, NAO, and the Antarctic Oscillation—AAO), and for the solar flux (SF) to adjust the daily median partial columns in the MLT, following:

$$O_3(t) = Cst + x_{j=1} \cdot trend + \sum_{n=1,4} [a_n \cdot \cos(n\omega t) + b_n \cdot \sin(n\omega t)] + \sum_{j=2}^m x_j X_{norm,j}(t) + \varepsilon(t) \quad (1)$$

where t is the number of days, x_1 is the trend coefficient in the data, $\omega = 2\pi/365.25$. $X_{norm,j}$ are the m chosen

Table 1. List of the Proxies Used in This Study and Their Sources

Proxy	Description (Resolution)	Sources
$F_{10.7}$	The 10.7 cm solar radio flux (daily)	NOAA National Weather Service Climate Prediction Center: ftp://ftp.ngdc.noaa.gov/STP/space-weather/solar-data/solar-features/solar-radio/noontime-flux/penticton/penticton_adjusted/listings/listing_drao_noontime-flux-adjusted_daily.txt
QBO ¹⁰ QBO ³⁰	Quasi-Biennial Oscillation index at 10 hPa and 30 hPa (monthly)	Free University of Berlin: www.geo.fu-berlin.de/en/met/ag/strat/produkte/qbo/
ENSO	Multivariate El Niño–Southern Oscillation Index (MEI) (2 monthly averages)	NOAA National Weather Service Climate Prediction Center: http://www.esrl.noaa.gov/psd/enso/mei/table.html
NAO	North Atlantic Oscillation index (daily)	ftp://ftp.cpc.ncep.noaa.gov/cwlinks/norm.daily.nao.index.b500101.current.ascii
AAO	Antarctic Oscillation index (daily)	ftp://ftp.cpc.ncep.noaa.gov/cwlinks/norm.daily.aao.index.b790101.current.ascii
GEO	Geopotential height (daily)	http://apps.ecmwf.int/datasets/data/interim-full-daily/?levtype=pl
PV	Potential vorticity (daily)	

“explanatory variables,” also called “proxies” or “covariates” normalized over the period of available IASI observations used here (January 2008 to March 2016) with

$$X_{\text{norm}}(t) = 2[X(t) - X_{\text{median}}]/[X_{\text{max}} - X_{\text{min}}] \quad (2)$$

The coefficients a_n, b_n, x_j are the regression coefficients which quantify the effect of the seasonal and non-seasonal variables over the IASI period, and $\varepsilon(t)$ is the residual variation which is assumed to be autoregressive with time lag of 1 day. The constant term (Cst) and the regression coefficients are estimated by the least squares method. Their standard errors are calculated from the covariance matrix of the coefficients, and they are corrected to take into account the uncertainty due to the autocorrelation of the noise residual [see *Wespes et al.* [2016], equation (3)].

The regression model used here mainly differs from the one described in *Wespes et al.* [2016] in that it includes additional proxies describing the geopotential height (GEO) and the potential vorticity (PV) at 200 hPa and also it allows for 3- and 4-month seasonality ($n = 3$ and 4 , respectively) in addition to the 1-year and 6-month ($n = 1$ and 2 , respectively) to describe oscillation patterns on shorter timescales. The GEO and PV proxies are used to account for the tropopause height and the mixing of tropospheric and stratospheric air masses, respectively. The effect of the El Niño–Southern Oscillation is parameterized here by the Multivariate ENSO Index (MEI) which relies on a combination of parameters: sea surface temperature anomalies, sea level pressure anomalies, zonal and meridional surface winds, surface air temperature, and cloud fraction over the tropical Pacific [*Wolter and Timlin*, 2011]. The other proxies (QBO, NAO, AAO, and SF) used to describe the variations in MLT O_3 records are the same as those described in *Wespes et al.* [2016]. The selected proxies are listed in Table 1 along with their sources and their resolutions. Note that the NAO and AAO indexes are used for the N.H. (Northern Hemisphere) and the S.H. (Southern Hemisphere), respectively, while both are used for the equatorial band ($10^\circ\text{S}–10^\circ\text{N}$). The time series of the main ones normalized over the 2000–2016 period are illustrated in Figure 4.

Because of the altitude-dependent lag for the QBO signal [e.g., *Randel and Wu*, 1996], we use two orthogonal functions at 10 and at 30 hPa which show strong anti-correlation and which are sufficient to account for both the strength and the phase of QBO. This allows the regression model to adjust the time lag, and it also avoids preselecting an optimal lag for the O_3 fitting. On the contrary, for accounting the possible time lags relation between ENSO and the O_3 response [e.g., *Zeng and Pyle*, 2005], we have tested different time lags ranging from 1 to 4 months (referred as lag-1 to lag-4) in the regression model. Because 2-month averages were used for building the MEI index and, as a consequence, for avoiding possible compensation effects in the O_3 time series adjustment between successive 1-month time lags, we only retain the ENSO lag-2 and lag-4 in addition to the non-lagged one (lag-0), which are found to give a good representation of the IASI O_3 records (see section 4.2).

Since the proxies may differently influence O_3 across the seasons, the seasonality in the regression coefficients is also examined in this study by splitting the *annual* model (equation (1)) into four seasonal functions which then produces a *seasonal* model in which each adjusted proxy $x_j X_{\text{norm},j}$ is replaced by $x_{\text{spr}} X_{\text{norm},\text{spr}} + x_{\text{sum}} X_{\text{norm},\text{sum}} + x_{\text{fall}} X_{\text{norm},\text{fall}} + x_{\text{wint}} X_{\text{norm},\text{wint}}$. Finally, using both the annual (where $x_{\text{spr}} = x_{\text{sum}} = x_{\text{fall}} = x_{\text{wint}}$)

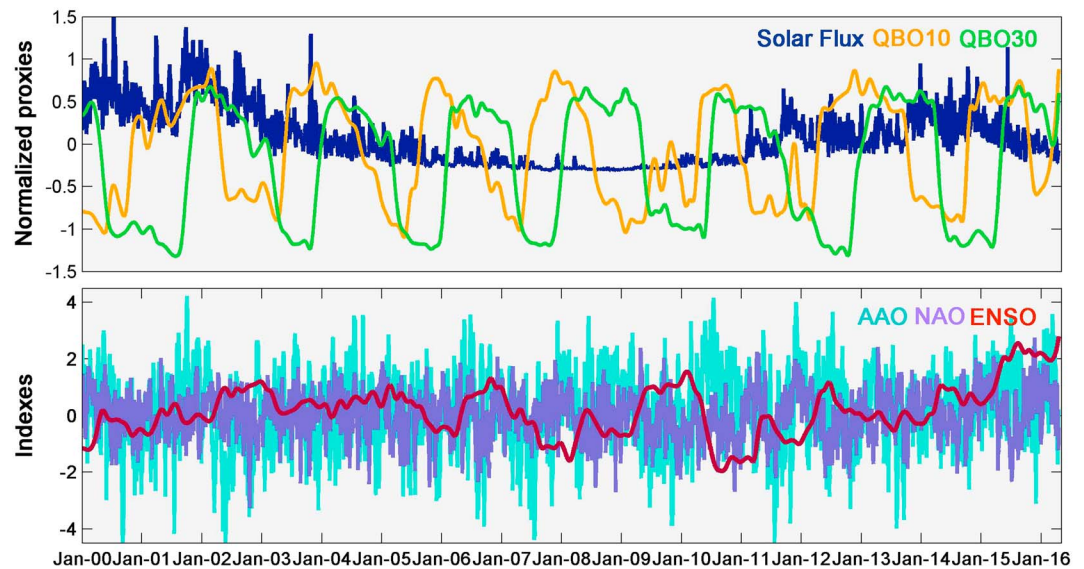


Figure 4. (top) Normalized proxies as a function of time for the period from January 2000 to March 2016 for the $F_{10.7}$ cm solar radio flux (dark blue) and the equatorial winds at 10 (orange) and 30 hPa (green), respectively, and (bottom) indexes for the El Niño Southern (red), North Atlantic (purple), and Antarctic oscillations (light blue).

and seasonal models, we estimate the coefficients x_j separately for each grid cell and provide global maps of the estimates for each O_3 regressor.

For the assessment of the best combination of the variables to be adjusted for each grid cell in the regression model, we perform an iterative stepwise backward elimination method, similar to previous studies [e.g., Steinbrecht *et al.*, 2004; Mäder *et al.*, 2007, 2010; Knibbe *et al.*, 2014; Wespes *et al.*, 2016]. Only the variables that have influence on the IASI O_3 variations with a high significance value (chosen as $>95\%$) are retained in the model. The initial model includes all the proxies listed in Table 1. During the iterative phases, the variable characterized by the largest p value exceeding a significance level α of 0.05 is rejected. At the end of the process, all p values are below α and the retained variables are considered to significantly drive the IASI O_3 variations. Their standard errors are also a posteriori corrected to take into account the uncertainty due to the autocorrelation of the noise residual.

3. Evaluation of the Regression Models (Annual and Seasonal)

3.1. Comparison Between IASI and the Regression Models

Figure 5 presents the annual (Figure 5a) and the seasonal (Figure 5b) distributions for two periods (December–February and March–May) of tropospheric O_3 measured by IASI averaged over January 2008 to March 2016 (left), along with the associated model residuals (middle) and the part of the variability in IASI data which is explained by the regression models (right), as calculated from $\frac{\sigma(O_3^{\text{Fitted_model}}(t))}{\sigma(O_3(t))}$, where σ is the standard deviation relative to the fitted regression models (annual and seasonal) and to the IASI O_3 time series. The seasonal patterns (the June–August and September–November periods are not shown here) averaged over the 8 years of IASI are very close to those previously illustrated for the year 2014 in Figure 1 indicating that the processes described above in section 2.1 (maximum in tropospheric O_3 records in spring-summer in the midlatitudes of the N.H., high O_3 values over the highly populated areas of Asia and over the eastern part of the Mediterranean Basin during summer, and large fire activity in spring over central Africa) are recurrent over the period of the IASI observations. This also explains the weak anomalies calculated above these regions (see Figure 3, anomaly $< 10\%$). The distributions of the residuals and of the contribution explained by the models show that the regression models reproduce well the daily median of IASI observations with no observed bias (relative differences $< 1\%$ in almost all situations for the two models) and that they explain a large fraction (from $\sim 40\%$ to $\sim 90\%$) of the variation in the daily O_3 IASI data set, especially in the N.H. and in the tropics (70% – 90% on average for the annual model). These two regions are of particular interest in

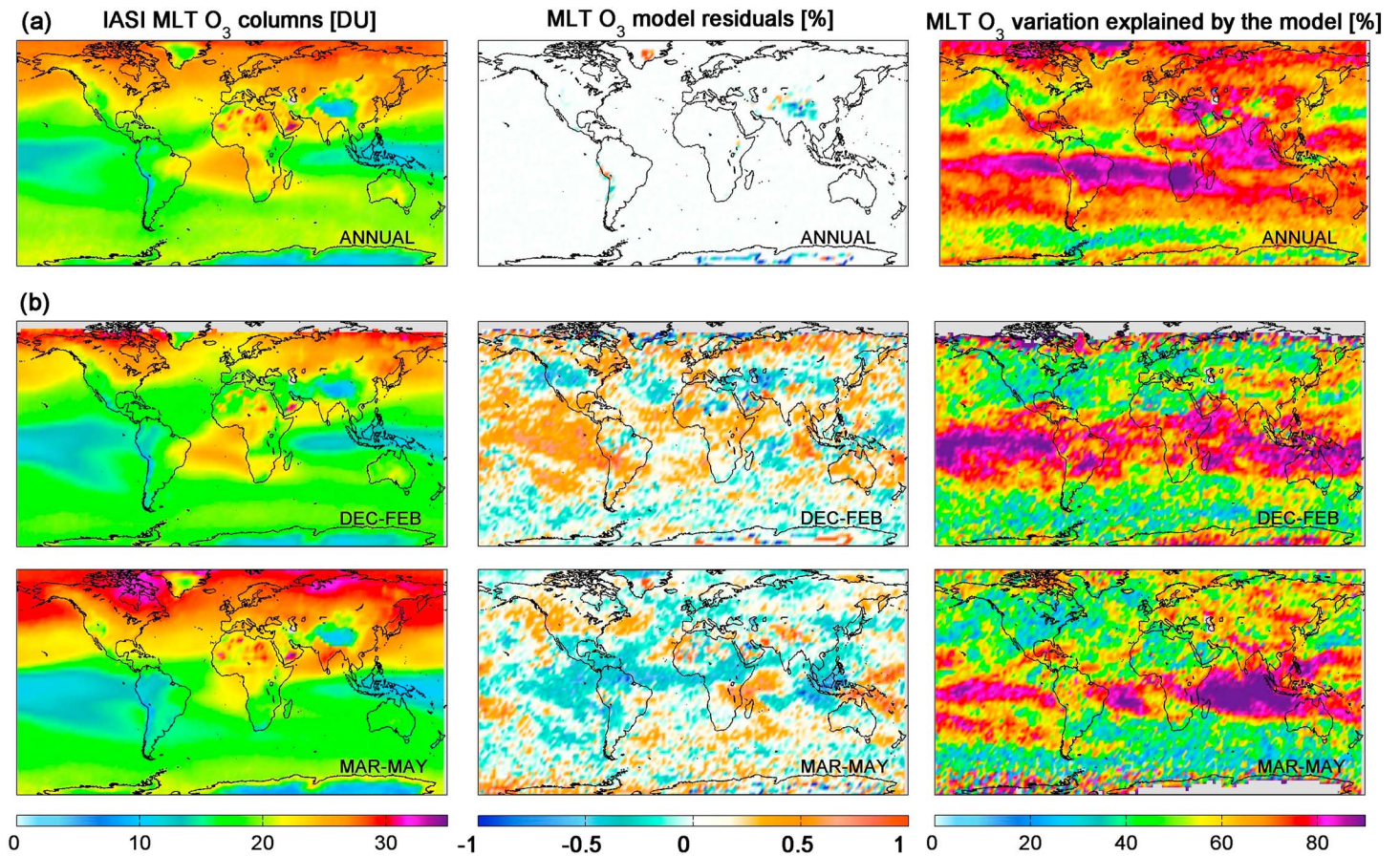


Figure 5. (a) Global distribution of O₃ tropospheric columns (in Dobson unit) measured by IASI and averaged over January 2008 to March 2016 (left) of the regression model residuals calculated as follows: $[100(\text{IASI} - \text{model})/\text{IASI}]$ (in percent) (middle) and of the fraction of the variation in IASI data explained by the regression model, calculated as $[100 \times (\sigma(\text{O}_3^{\text{fitted_model}}(t))/\sigma(\text{O}_3(t)))]$ (in percent). Data are averaged over a $2.5^\circ \times 2.5^\circ$ grid box. (b) Same as (Figure 5a) but for the seasonal distributions for two periods (December–February and March–May).

this study given their high IASI sensitivity and their high anomalies (>25% in the tropics), respectively (see section 2.1 and Figures 1 and 3). The weakest performance of the models is located around the Antarctic during spring (September–November period, not shown here) with contributions lower than 30% on average. This is likely due to the intense variations in the O₃ MLT columns during the vortex deployment which is not parameterized in this study.

3.2. Fitting Performances of Annual Versus Seasonal Model

Figures 6a and 6b present global distributions of MLT O₃ adjusted by the annual regression model and by the seasonal one, respectively. The consistency between the two models and their quality fit are then evaluated at the end of the stepwise iterative process by comparing the two raw residuals (Figure 6c) and the Pearson’s goodness of fit statistic (Figure 6d) calculated as $\chi^2 = \sum_t r_t^2$, where $r = \frac{\text{O}_3(t) - \text{O}_3^{\text{fitted}}(t)}{\text{RMSE}}$ is the standardized

Pearson residual, O₃(t) the IASI daily median, O₃^{fitted}(t) the adjusted value, and RMSE the root-mean-square error of the regression fit, which allows to estimate how well do the observed data correspond to the adjusted models. To this end, the chi-squared differences between the two models $\Delta\chi^2 = \chi_{\text{annual}}^2 - \chi_{\text{seasonal}}^2$ are calculated. This statistical chi-squared test is particularly useful to evaluate the performances of two nested parametric models which differ by an arbitrary set of coefficients, one being an extended version of the other one (in our case, the seasonal model— M_{seasonal} —being the extended one and the annual model— M_{annual} —the restricted one) [e.g., Chandler and Scott, 2011; Wilks, 2011; Christensen, 2015]. It allows testing that the null hypothesis H_0 (in our case M_{annual}) is true, meaning that M_{seasonal} brings no improvements. Since a small value

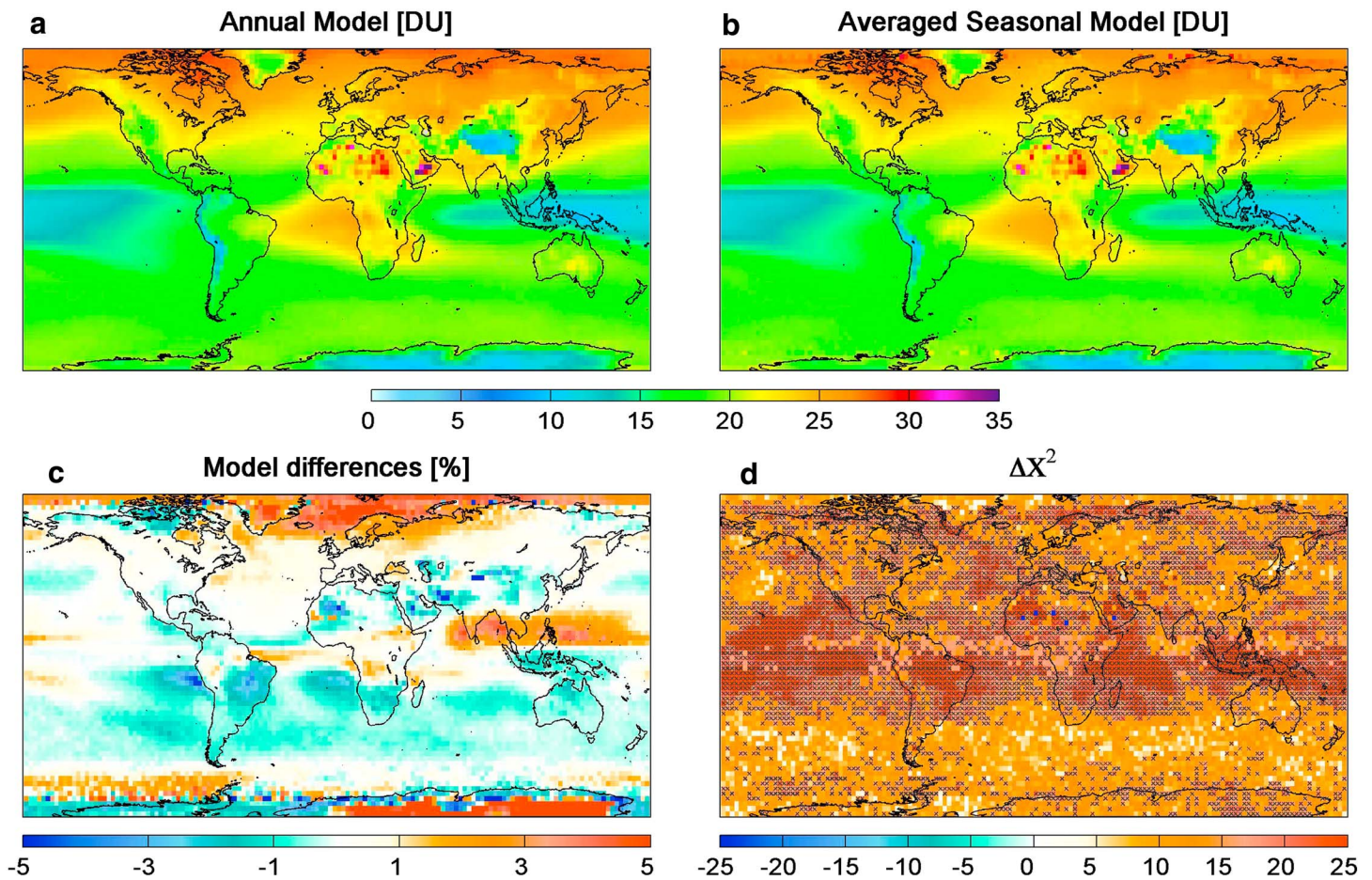


Figure 6. Global distributions of O₃ tropospheric columns adjusted (a) from the annual regression model (M_{annual}) and (b) from the seasonal regression model (M_{seasonal}), averaged over January 2008 to March 2016. The global distributions (c) of the differences between the annual and the seasonal regression models calculated as follows: $[100 \times (M_{\text{annual}} - M_{\text{seasonal}}) / M_{\text{seasonal}}]$ (in percent) and (d) of the differences in the Pearson's goodness of fit statistic between the two models [$\Delta X^2 = X^2_{\text{annual}} - X^2_{\text{seasonal}}$] (see text for details). ΔX^2 values marked with scatters refer to rejection of the annual model in favor to the seasonal one at the 10%-level. Data are averaged over a $2.5^\circ \times 2.5^\circ$ grid box.

of X^2 characterizes a good fit, positive values of ΔX^2 provide evidence against the “restricted” annual model in favor of the “extended” seasonal one. Even if Figure 6c indicates a good consistency between the two models with relative differences, calculated as $100 \times \frac{M_{\text{annual}} - M_{\text{seasonal}}}{M_{\text{seasonal}}}$, usually below 3% (except over Antarctica), Figure 6d shows that 97.7% of the global grid cells are characterized by a positive ΔX^2 and, therefore, that a better fit is performed with the seasonal model. To better estimate the probability that the additional parameters in M_{seasonal} bring statistically significant information at a specific confidence level, we perform the likelihood-ratio test statistic. This test consists in comparing the chi-squared differences ΔX^2 (Figure 6d) to a theoretical asymptotic X^2_{p-q} distribution with $p-q$ degrees of freedom, where p and q are the numbers of parameters in M_{seasonal} and M_{annual} , respectively, at a significance level α . If the computed ΔX^2 exceeds the theoretical value $X^2_{p-q}(1 - \alpha)$, the null hypothesis is rejected. This test indicates that the seasonal model is preferred to the annual one at the 10% level α for 46.4% of the grid cells (marked with scatters in Figure 6d). These cells correspond to those with the largest ΔX^2 which are mostly found in the tropical band and in some regions of the N.H. This indicates a higher probability to achieve more physically meaningful patterns when M_{seasonal} is used but only above these regions. Since a preference for the seasonal model at the global scale is not demonstrated, the annual model is analyzed first in sections below for simplification purposes. It is then completed with the seasonal model to help in further interpreting the IASI O₃ variations especially in the tropics and in the N.H.

We also performed checks on the residuals to verify the absence of typical deviation (e.g., curvature and changes in the range of the residuals; not shown here). The impact of the spatial sampling on the quality fit has also been assessed by performing the regression models on several grid resolutions. The regression results in terms of fitted patterns, residuals, and variations are fully consistent between the different tested resolutions (e.g., $1^\circ \times 1^\circ$, $5^\circ \times 5^\circ$ and $10^\circ \times 10^\circ$ grid cells; data not shown here), which highlights the robustness of the two regression models and fitting procedure. Finally, the misleading enhanced O_3 values which are retrieved above the deserts (see section 2.1) are filtered out for all further analyses using the *RMSE* of the regression fits. The latter is lower than 5 DU almost everywhere (not shown here), except above deserts where it reaches 15 DU.

4. Patterns of Geophysical Variables: Results and Discussion

In this section, the spatial patterns of the regression coefficients for the main seasonal and non-seasonal variables (i.e., harmonic and proxy terms) obtained according to the elimination procedure described in section 2.2 are shown on a $2.5^\circ \times 2.5^\circ$ resolution grid. The regression has also been applied on different spatial samplings to verify the consistency of the spatial information on O_3 -regressor dependencies. The results obtained for the different resolutions are fully consistent, and the $2.5^\circ \times 2.5^\circ$ resolution grid was considered as the best compromise between the resolution and the quality fit.

4.1. Seasonal O_3 Variations

Figure 7a presents the global distributions of the adjusted coefficients in the annual regression model for the 1-year harmonic terms (see equation (1) and section 2.2). The regression coefficients are scaled by the fitted constant term for clarity. The crosses in Figure 7 indicate that the regression coefficient in the grid cell is non-significant in the 95% confidence limits (2σ level) when accounting for the autocorrelation in the noise residual at the end of the elimination procedure. The associated standard errors in the 95% confidence limit for the retained variables, as well as the contribution of 1-year and 6-month seasonalities into the IASI O_3 variations which is estimated as $\frac{\sigma([a_n \cos(n\omega t) + b_n \sin(n\omega t)])}{\sigma(O_3(t))}$ where σ is the standard deviation relative to the fitted signal of the harmonic terms and to the IASI O_3 time series, are also represented (Figures 7b and 7c). We find clear hemispheric significant differences in the regression coefficient distributions with, on average, positive (or negative) signs, associated with small standard errors ($<20\%$), for the annual terms (a_1 and b_1 ; see equation (1)) in the N.H. (or S.H.). They correspond to annual maxima observed in spring-summer in midlatitudes and in winter-spring in high latitudes. The increase in the amplitude of the coefficients and in the explained contribution from middle to high latitudes of the N.H. likely reflects the cycle induced by the Brewer-Dobson circulation. The annual variation is modeled as the main driver of the observed O_3 variability with contributions larger than 50% almost everywhere, except over Antarctica where the annual seasonality is perturbed by the O_3 polar chemistry, and around the intertropical convergence zone where the coefficients become non-significant. The annual contribution is modulated at a more regional scale by the adjustment of the 6 month harmonic terms (a_2 and b_2 ; see equation (1)), with, on average, negative coefficients (data not shown) and large contributions to the IASI variation ($>45\%$) over Indian/western Pacific Oceans (Figure 7c) which are also the regions characterized by the strongest anomalies (see Figures 2 and 3 and section 2.1). Variations on shorter time scales (3 month and 4 month) are only found over restricted regions in the intertropical band and contribute only slightly ($<20\%$) to the O_3 variability with large standard errors ($>50\%$) (not shown). Finally, note also that a high spatial stability of the regression model and procedure is found with a clear distinction between the regions characterized by significant regression coefficients and by non-significant coefficients (represented by crosses and white grid cells).

4.2. Non-seasonal O_3 Variations

The regression coefficients for the explanatory variables which are retained in the annual regression model, as well as their IASI O_3 contributions which are calculated as $\frac{\sigma(x_j X_{norm,j})}{\sigma(O_3(t))}$, where σ is the standard deviation relative to the fitted signal of the proxies and to the IASI O_3 time series, are shown in Figures 8 and 9, respectively. As for the non-seasonal parameters, the areas of significant drivers (in the 95% confidence limit) are surrounded by non-significant cells when accounting for the autocorrelation in the noise residual. The solar flux, AAO, PV, and GEO proxies are generally minor components with relative contribution smaller than 10%

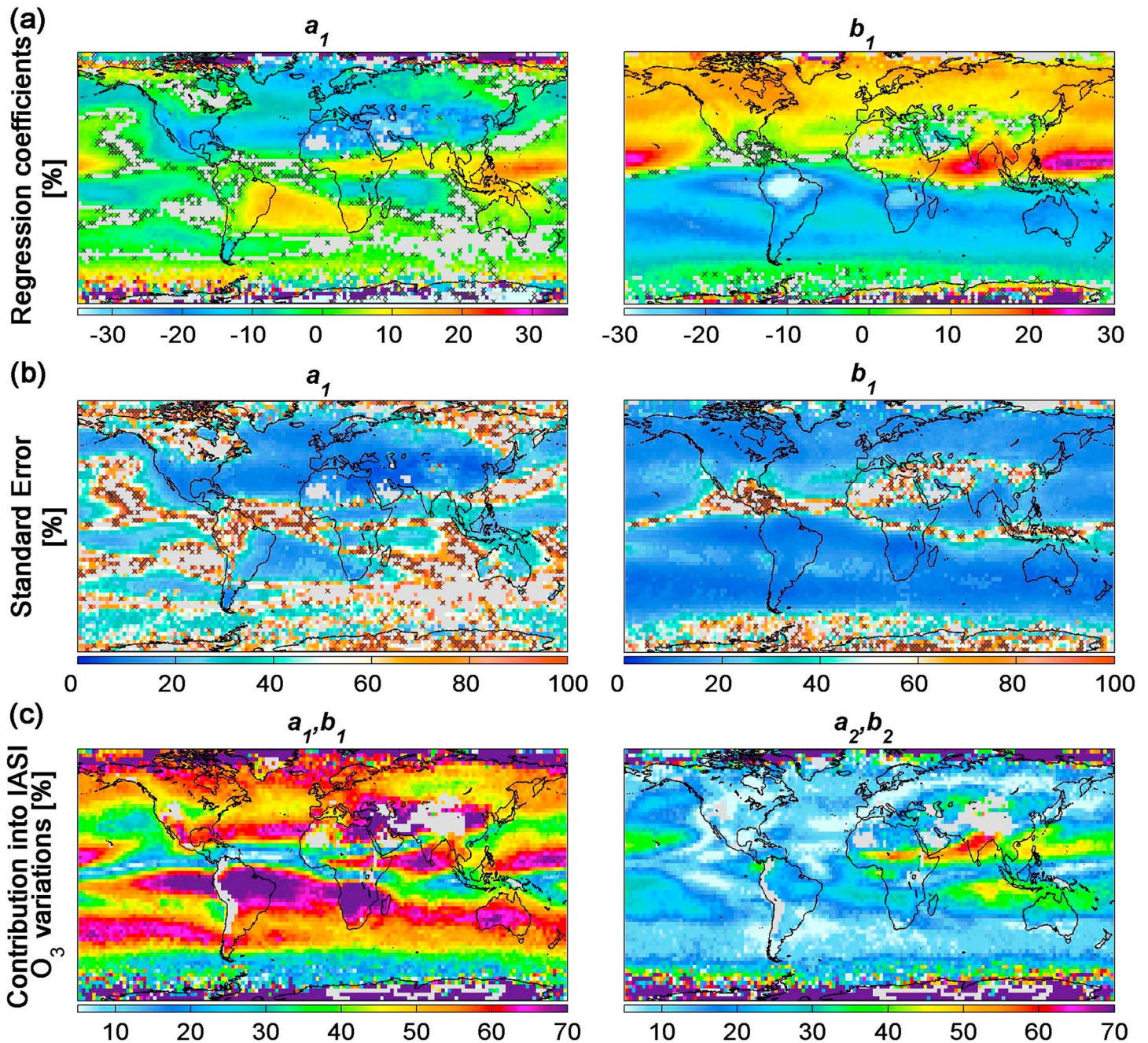


Figure 7. Global distribution (a) of the fitted regression coefficients for the 1-year (a_1, b_1) harmonic terms (see text, equation (1), for details) from the annual model and (b) of their associated standard errors (in the 95% confidence limit) (in percent). (c) Global distribution of the contribution for the 1-year (a_1, b_1) and 6-month (a_2, b_2) seasonalities into the IASI O₃ variations estimated as $[100 \times \sigma(a_n \cos(n\omega t) + b_n \sin(n\omega t)) / \sigma(O_3(t))]$ (in percent).

and large standard errors ($>80\%$, not shown). The results are not shown for the PV and GEO proxies which are only retained in the procedure for a few grid cells. The proxies are all characterized by regions of correlation (positive coefficients) or anti-correlation (negative coefficients) with the IASI O₃ time series.

Since only daytime O₃ IASI observations are used in this study, only small areas are identified with significant influence from the AAO which is related to the strength of the polar vortex in the S.H. [Thompson and Wallace, 2000; Frossard et al., 2013; Rieder et al., 2013]. We observe, nevertheless, latitudinal differences in the regression coefficients with negative coefficients in the tropics and positive ones in the extratropics. This is possibly

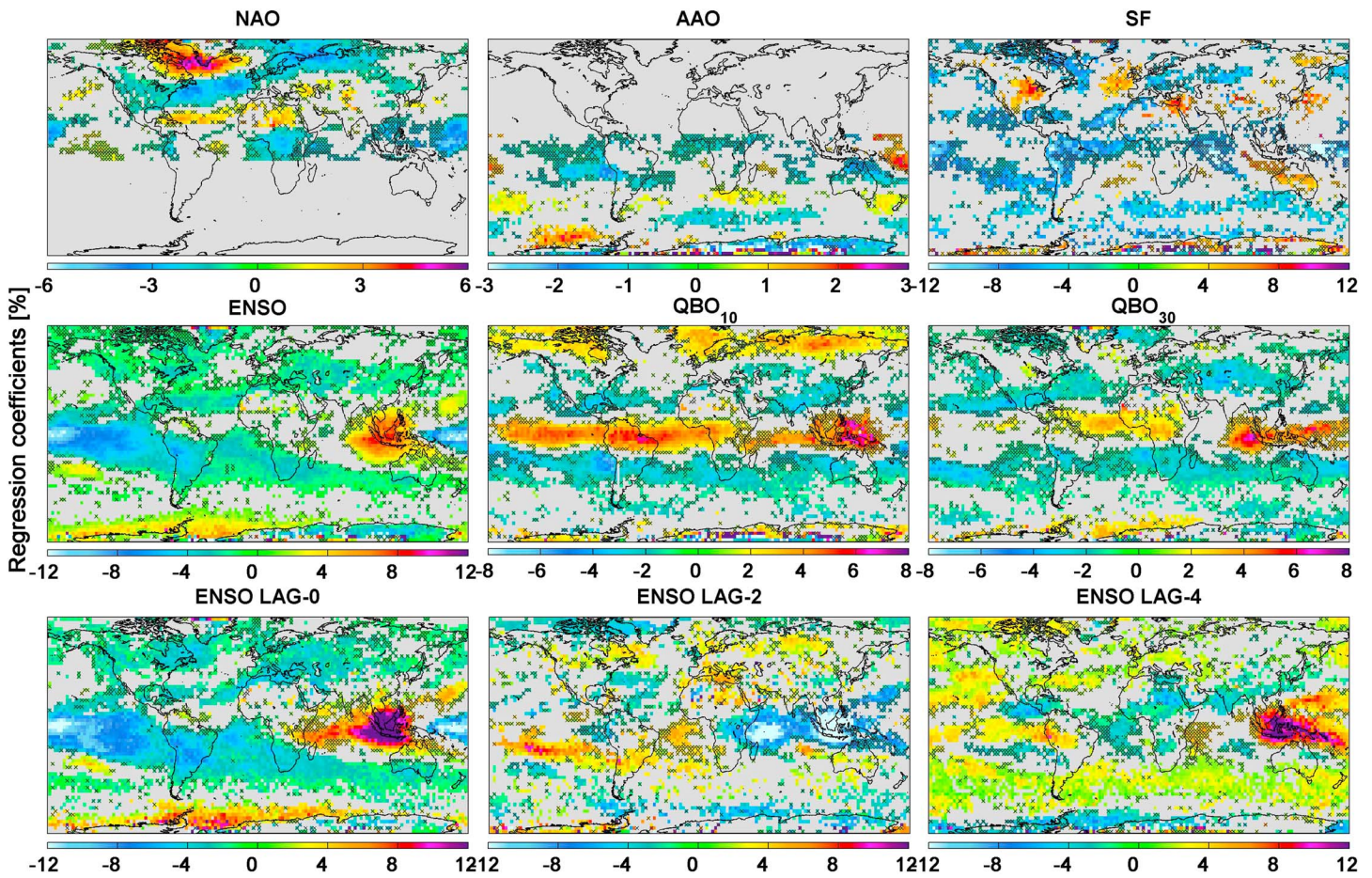


Figure 8. Global distribution of the fitted regression coefficients for the non-seasonal variables $[100 \times \sigma(x_j X_{norm,j}) / \sigma(O_3(t))]$. Identification for the variables: solar $F_{10.7}$ cm radio flux: SF, quasi-biennial oscillations at 10 and 30 hPa: QBO10 and QBO30, Antarctic oscillation: AAO, North Atlantic oscillation: NAO, and El Niño–Southern Oscillation: ENSO (without lags). ENSO proxies from fit including time lags of 0, 2, and 4 months (ENSO lag-0, lag-2 and lag-4) are also represented. Note that the scales are different.

linked to the transport of O_3 -rich air from the tropics to the polar region associated with enhanced wave activity in the tropics [e.g., Frossard et al., 2013; Rieder et al., 2013].

Even if most of the solar cycle variation of ozone occurs in the stratosphere [e.g., Soukharev and Hood, 2006], the coarse vertical resolution of IASI (see section 2) is such that upper and lower atmospheric levels contribute to each other making the use of the solar flux proxy justified when adjusting O_3 time series in the troposphere. Because of that mixing of tropospheric and stratospheric layers as seen by IASI, the interpretation of the fitted solar cycle effect is complex. The solar cycle is found to have some significant negative effects on annual O_3 changes in tropical and midlatitudes regions. This is in contradiction with previous studies which reported, from a combination of nadir-viewing and limb-sounder observations used to improve the O_3 vertical resolution in the lower stratosphere, a positive annual O_3 response in the lower stratosphere (> 100 hPa) to the solar cycle consistent with its strongest influence on changes in lower stratospheric dynamics in these regions [e.g., Soukharev and Hood, 2006; McCormack et al., 2007]. Nevertheless, changes in photochemistry in the tropical source region or indirect upper stratospheric solar effects on the development of the dynamics in the lower stratosphere/upper troposphere [Hood, 1997; Kadera and Kuroda, 2002; Hood and Soukharev, 2003; Austin et al., 2007] may also influence the O_3 response. Note, however, that the full understanding of these mechanisms has not yet been achieved.

The geophysical patterns for the other proxies, NAO, QBO10/30, and ENSO, show clear evidence of strong dynamical contribution to the tropospheric O_3 variability with large significant regional differences in the regression coefficients.

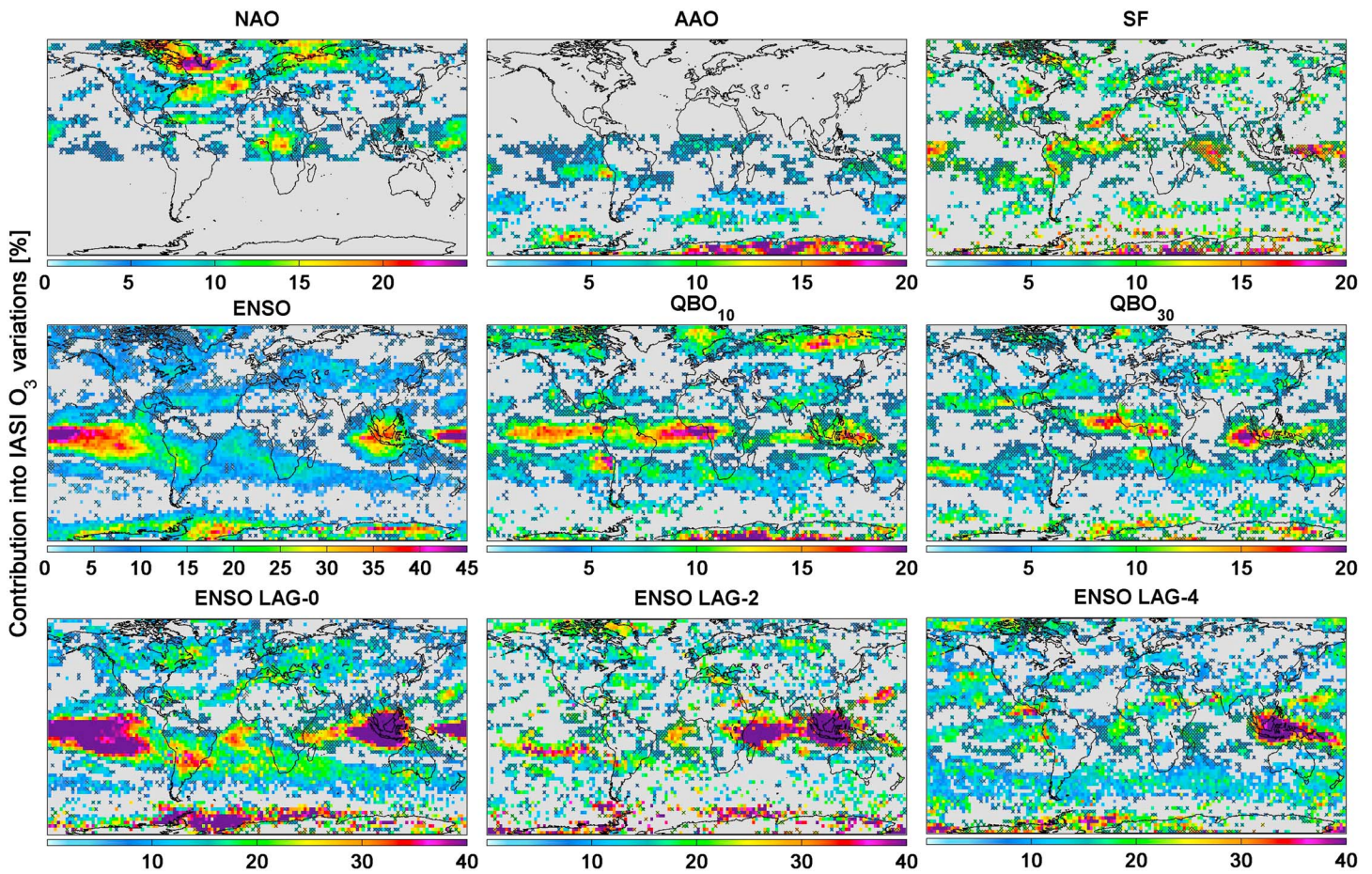


Figure 9. Same as Figure 8 but for the contributions of the fitted regression coefficients for the non-seasonal variables into the IASI O₃ variations estimated as $[100 \times \sigma(x_j X_{\text{norm},j}) / \sigma(O_3(t))]$.

1. NAO. It presents a significant characteristic dipole in the adjusted coefficients between the Labrador/Greenland (positive coefficients) and the North Euro-Atlantic (negative coefficients) sectors. This is fully consistent with opposite sea level pressure anomalies over the Icelandic/Arctic region and over the subtropical Atlantic region that induce the NAO oscillation [Hurrell, 1995]. It is also in agreement with previous studies which investigated the correlations between tropospheric ozone and the NAO [e.g., Creilson et al., 2003]. The positive coefficients over Labrador account for the increase (or decrease) in tropospheric O₃ records during the positive (or negative) phase of the NAO, while the contrary is observed for regions of negative coefficients. The positive phase of the NAO is characterized by stronger westerlies across the midlatitudes which are induced by low-pressure anomalies over the Icelandic/Arctic regions and high-pressure anomalies over the subtropical Atlantic. The relative contributions for that covariate reach 25% over Labrador. The dipole in the NAO coefficients is also observed on a seasonal basis, especially during the winter. This is illustrated in Figure 10 which represents the seasonality for the main contributing dynamical variables for two periods (from December to February—DJF and from June to August—JJA; see Figures 10a and 10b, respectively) adjusted from the seasonal model (M_{seasonal} ; see section 2.2). Interestingly, we find that this result is in agreement with Thompson and Wallace [2000] who describes a pronounced seasonality of the Northern Hemisphere annular mode (NAM) and shows that it is more clearly defined during the winter.
2. QBO. On both annual (Figure 8) and seasonal (Figure 10) basis, the regression coefficients combined with their standard errors indicate that the QBO has a strong significant influence on tropospheric O₃ in the tropics, where it is known to be an important dynamical driver of O₃ variations through convective anomalies [e.g., Chipperfield et al., 1994; Randel and Wu, 1996, 2007; Logan et al., 2003; Fishman et al., 2005; Tian et al., 2006; Witte et al., 2008; Neu et al., 2014]. In particular, the band-like structure of high

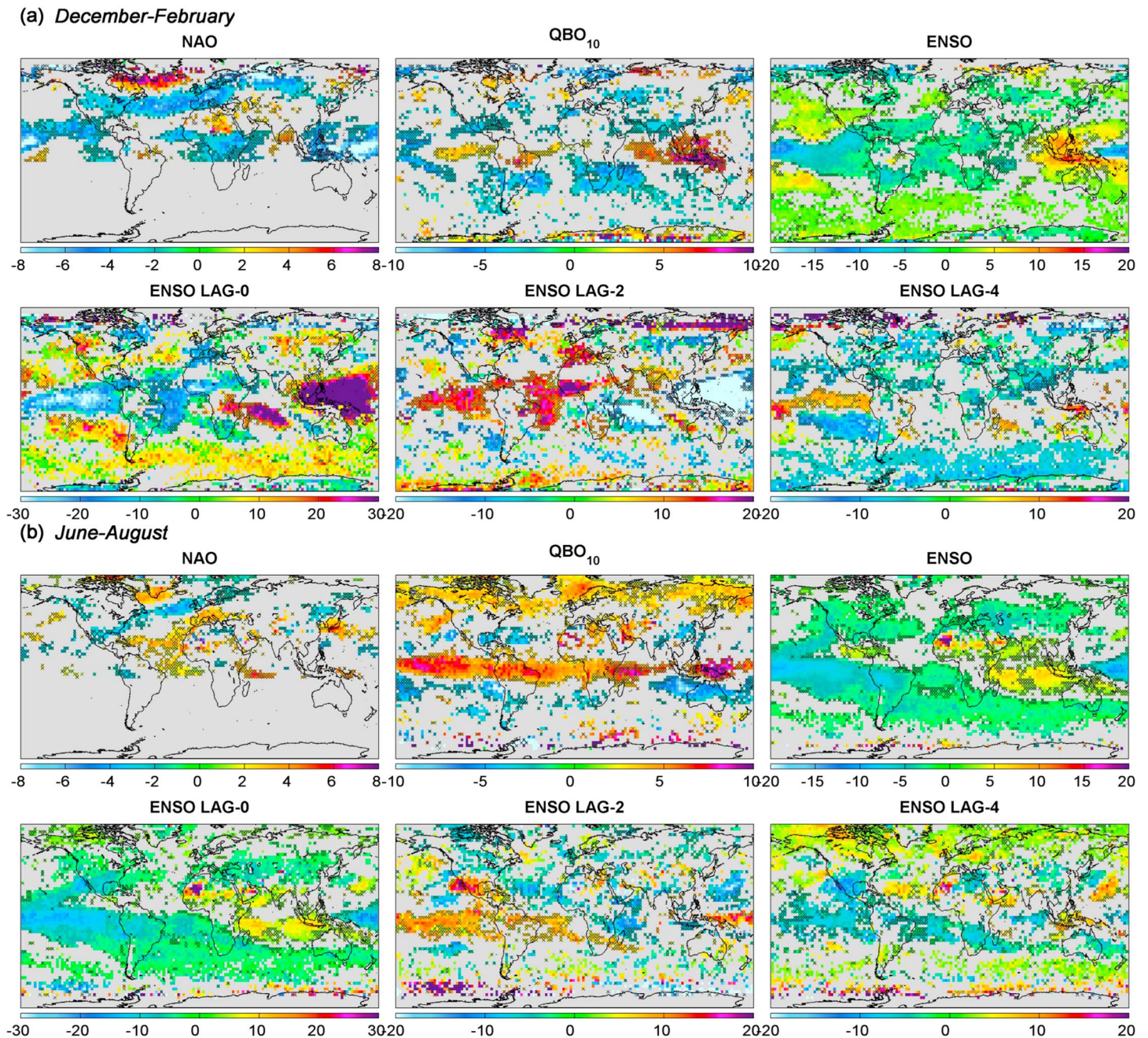


Figure 10. Same as regression coefficient distributions of Figure 8 but only for the main proxies: NAO, QBO10, ENSO (from fit with no lags), and ENSO lag-0, lag-2 and lag-4 from the seasonal model for (a) the DJF and (b) the JJA periods. Note that the scales are different for the proxies.

positive coefficients around the equator and the sharp meridional gradient likely reflect the QBO-related deep convection at the equator which traps the chemical species, favors the upward transfer in that region, and induces more time for the air masses to mix with midlatitudes [Li et al., 2005; Flury et al., 2013]. The QBO is modeled to be a major contributor in that region with a relative contribution of the sum of the two adjusted QBO components (QBO10+QBO30) to the O₃ changes reaching 45% on an annual basis.

The QBO is also shown to affect the tropospheric O₃ flow toward the poles. It is particularly interesting to see that the sharp equatorial-extra-equatorial gradient (with positive coefficients turning negative) and that the smoother positive gradient from the extra-equatorial regions to the poles (with negative coefficient turning

positive) are in line with the meridional distribution of the zonal wind shear anomalies [see *Huesmann and Hitchman, 2001*]. Hence, the high-latitude QBO-driven O₃ maxima here identified likely support previous studies that invoke a QBO modulation of large-scale planetary waves and interactions with the Brewer-Dobson circulation [e.g., *Baldwin et al., 2001*; *Bönisch et al., 2011*; *Salby and Callaghan, 2006*; *Flury et al., 2013*].

3. ENSO. It is mostly governed by sea surface temperature (SST) anomalies in the Niño region 3.4 (region bounded by 120°W–170°W and 5°S–5°N). As a consequence, it shows a contrast in the regression coefficients between tropical (negative coefficients) and extratropical (coefficients turning positive) regions (see Figure 8; ENSO panel from the adjustment of the annual and seasonal models without ENSO time lags), especially during the DJF period (see Figure 10a), with exception over Indonesia/North Australia where a positive impact on O₃ changes is modeled. This is likely explained by both dynamical and chemical effects induced by El Niño events. Although increased convection during the positive phase of the ENSO leads to a decrease in tropospheric O₃ in the Niño region (negative coefficients) [*Newman et al., 2001*; *Randel et al., 2002*], we also find an increase in emissions of O₃ precursors from Indonesian and Australian fires (positive coefficients) explained by reduced rainfalls during El Niño conditions [e.g., *Worden et al., 2013*]. This distribution of the regression coefficients is fully in agreement with previous studies which showed a relationship between satellite-derived tropospheric O₃ and the phase of the ENSO cycle in the tropics [e.g., *Fishman et al., 1990*; *Ziemke and Chandra, 2003*; *Fishman et al., 2005*] and, more particularly, which reported that El Niño events conduct an increase in tropospheric O₃ over western Pacific/Indonesia/North Australia and a decrease over the central and eastern Pacific [e.g., *Oman et al., 2013*; *Valks et al., 2014*; *Ziemke et al., 2014*]. The ENSO is shown to be the largest contributor compared to all other dynamical covariates, and interestingly, the pattern of its contribution into the IASI O₃ variations shows clear correlation with that of the deseasonalized anomalies in the MLT (see Figure 3 and section 2.1). The strongest relative contribution of ENSO reaches 55% over the west Pacific region and is in agreement with the location and the magnitude of the maximum variance explained by the ENSO influence reported in *Olsen et al. [2016]* from the assimilation of satellite observations of tropospheric O₃. The ENSO also explains 40% of IASI O₃ variation over the Indonesian fires region. We also observe a seasonality in the regression coefficients with a larger range during the DJF and MAM (March–May; data not shown) periods than during JJA, and hence a larger contribution to the IASI variance during winter-spring, which is in line with the maximum ENSO activity in winter.

A time lag relation between ozone and the ENSO variable is also investigated on both annual and seasonal basis. It results from additional adjustments where ENSO was split into three different proxies (zero-lag, 2-month and 4-month lags; see section 2.2). Sensitivity tests, similar to those conducted in section 3.2, for including or not, in the annual and the seasonal regression models, these possible lags in the O₃ response have been performed. For the annual regression, the tests indicate that the model including time lags, $M_{\text{annual_with_lags}}$, improves the quality of the adjustment for 65.5% of the grid cells, with a positive ΔX^2 calculated as $X^2_{\text{annual_w/o_lags}} - X^2_{\text{annual_with_lags}}$, and that it is significantly preferred to the reduced non-lagged model, $M_{\text{annual_w/o_lags}}$, for 41.3% of grid cells as calculated from the chi-squared statistic in the 10%-level. Including ENSO time lags in the seasonal model, $M_{\text{seasonal_with_lags}}$, also improves the fit with a positive ΔX^2 ($X^2_{\text{seasonal_w/o_lags}} - X^2_{\text{seasonal_with_lags}}$) for 88.5% of the cells. The likelihood-ratio test indicates that $M_{\text{seasonal_with_lags}}$ is preferred for 51.7% of the grid cells in the 10%-level, especially in the equatorial band and in high latitudes of the N.H. (not shown here) and, hence, that the time-lagged regression interestingly brings additional information over these regions. This is exploited by examining the ENSO time-lagged regression results on both annual and seasonal basis (see the ENSO lag-0, lag-2 and lag-4 distributions in Figures 8 and 10). Despite the fact that possible compensation effects between the fitted ENSO lag-2 and ENSO lag-0 and lag-4 are suspected, mainly over Indonesia where exactly opposite regression coefficients are found, and hence that it may overestimate their regression coefficients and their contributions to the O₃ variations, positive ENSO lag-2 and ENSO lag-4 signals are detected downwind Indonesia across west Pacific (see Figures 8 and 9). The lag-4 coefficients distribution from both the annual (Figure 8) and the seasonal regressions for the JJA period (Figure 10b) also shows that ENSO significantly affected air masses can even propagate further over middle and high latitudes of both hemispheres but with a smaller fitted amplitude and explained variation compared to the non-lagged ENSO in the tropical band. The fact that significant positive coefficients for ENSO lag-4 computed over the higher latitudes are

highlighted for the June–August (Figure 10b) period and amplified in comparison with the annual regression results (Figure 8) further indicates a possible time lag relation of several months in the tropospheric O₃ response to ENSO far from the Niño region.

The ENSO influence on tropospheric O₃ in the extratropics may reflect the O₃ response associated with specific tropospheric and stratospheric pathways which are connected with the ENSO changes in the tropics, which alter the tropospheric circulation and which impact on the O₃ levels over the middle and high latitudes [e.g., Langford, 1999; Zeng and Pyle, 2005; Koumoutsaris et al., 2008; Oman et al., 2013; Lin et al., 2014; Neu et al., 2014; Ebojie et al., 2016]. Butler et al. [2014] suggests a stratospheric pathway linking tropical Pacific SST anomalies to surface response primarily over the North Atlantic and Eurasian regions, which could explain that warm ENSO events induce enhanced O₃ concentrations in the extratropics. That pathway consists of planetary waves generation which results in sudden stratospheric warmings, in weak or disrupted polar vortex, and which, hence, impacts onto tropospheric circulation [e.g., Bronnimann et al., 2004; Butler et al., 2014, and references therein]. The tropospheric pathway results from the link between the ENSO phenomenon and the Pacific/North American (PNA) teleconnection pattern which is one of the most important natural modes of climate variability in the Northern Hemisphere extratropics. The positive phase of the PNA pattern is associated with the warm ENSO phase and with the strengthening and eastward extension of the East Asian subtropical jet stream into the midlatitude northeastern Pacific impacting over the North America [e.g., Franzke et al., 2011]. The ENSO impact on lower tropospheric O₃ has been identified in Lin et al. [2014] over the subtropical eastern Pacific in winter and spring. Oman et al. [2013] reported a significant positive tropospheric O₃ response to ENSO in the midlatitudes of both hemispheres using chemistry-climate model (CCM) and satellite measurements, but O₃ sensitivity of lagged ENSO signal was not examined. Olsen et al. [2016] tested time-lagged regressions on tropospheric column O₃ to ENSO in assimilated satellite data, but the regression results were not improved. An ENSO time lag has, however, been previously observed in Langford et al. [1998] and Langford [1999], which found correlations between free tropospheric ozone and El Niño following a several month (from 2 to 6 months) lag in lidar data from a site in Colorado, as originating from enhanced STE induced by ENSO. Despite the fact that ENSO-related tropospheric O₃ responses over tropical and extratropical regions have been reported in recent studies [e.g., Oman et al., 2013; Lin et al., 2014; Neu et al., 2014; Ziemke et al., 2015; Ebojie et al., 2016; Olsen et al., 2016], it is the first time that such a timing of the O₃ response is identified from satellite measurements, which constitutes an important finding of this study. Note, finally, that longer time lags for ENSO have been also tested in this study but without significant improvement on the fitting residuals. The ENSO signal in the IASI O₃ time series decreases everywhere after 4 months, except over the North Atlantic-Eurasian sector where a significant 6-month lagged ENSO contributing 20% to the IASI O₃ variations is observed. This finding is in line with Koumoutsaris et al. [2008] which identified a 6-month lag in the influence of El Niño on European tropospheric O₃ column using CCM. It could be linked to the stratospheric teleconnection pattern described in Butler et al. [2014], which suggests an ENSO impact mainly onto the North Atlantic and Eurasian regions in the troposphere, and it could correspond to the response time of STE [Langford et al., 1998; Zeng and Pyle, 2005]. It could also be related to the tropospheric pathway associated with an eastward extension of the subtropical jet stream during El Niño which enhances the Asian pollution export [e.g., Lin et al., 2014] and the transport toward Europe [Koumoutsaris et al., 2008].

4.3. NAO and ENSO Signals in O₃ Time Series

Figure 11 compares the 8 year time series of IASI O₃ daily averages with the results from the annual regression procedure (top row, dark blue and light blue, respectively) and shows as well the deseasonalised IASI and fitted time series calculated by subtracting the residuals and the modeled seasonal cycles (harmonic terms) from the time series (middle row) for four regions of interest: the Labrador Sea where a positive effect of the NAO on O₃ records is found (Figure 11a), Indonesia and the Equatorial Western Pacific (Figures 11b and 11c) which respectively show a positive ENSO “chemical” effect and a negative ENSO “dynamical” effect, and the North Western Pacific (Figure 11d) where an ENSO lag relationship is identified. The RMSE of the regression fits is also indicated. The fitted signals in Dobson unit for the main retained proxies are also represented (bottom row). For all the cases (Figures 11a–11d), signals for the NAO or ENSO oscillations are identified: their maximum responses (~8 DU for NAO, ~4.5–7 DU for ENSO) are larger than the RMSE (~4.3 DU for NAO and ~2.3–4 DU for ENSO) and they are characterized by large contributions (~28–58%), except for the lagged-4 ENSO in case (Figure 11d) which exhibits a smaller contribution (see section 4.2), and by reasonable

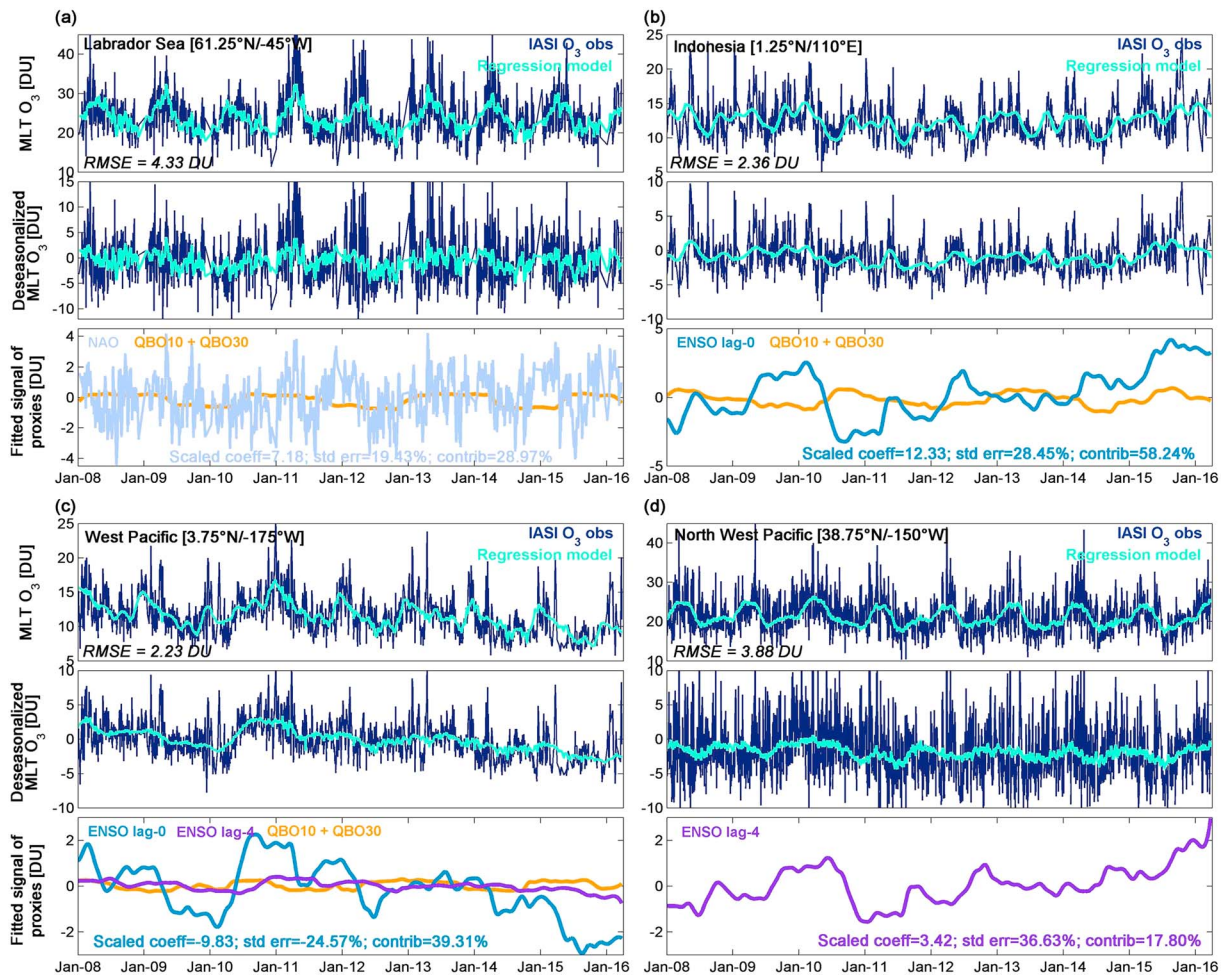


Figure 11. Daily time series of O₃ measured by IASI and adjusted by the annual regression model (top row), of the deseasonalized O₃ (middle row), and of the fitted signal of the main retained proxies calculated as follows: $[x_j X_{norm,j}]$ (bottom row) (given in Dobson unit) for four regions of interest: (a) Labrador sea (positive NAO effect), (b) Indonesia (positive ENSO chemical effect), (c) Equatorial Western Pacific (negative ENSO dynamical effect), and (d) North Western Pacific (lagged ENSO effect). The RMSE of the regression fits is also indicated.

standard errors in the 95% confidence limit (<35%). The highest O₃ records over the Labrador Sea (Figure 11a), a region of positive NAO coefficients, are observed during February–April of years 2011 and 2013 which correspond to a high peak in the positive phase of the NAO (monthly NAO index mean > 2; see Figure 4). Similarly, high O₃ levels (> 20 DU) in the IASI time series over Indonesia (Figure 11b) are found during moderate (bi-monthly ENSO index mean > 1.2 in winter 2009/2010) and strong (bi-monthly ENSO index mean > 2 in winter 2015/2016) El Niño episodes. Over the west Pacific region of negative coefficients (Figure 11c), the contrary is observed: a clear ENSO-like opposite signal is remarkably captured and is characterized by strong decreases in the O₃ levels consistent with the warmer ENSO phases during winters 2015/2016 and 2009/2010, followed by an increase during the cool La Niña episode in 2010/2011 (bi-monthly ENSO index mean < -1.5). Finally, a 4-month lagged ENSO signal is captured in the midlatitudes of the N.H. (Figure 11d) with an enlarged O₃ maximum in spring 2010, which coincides with a 4 month shift of the peak in the ENSO warm phase. This lag is possibly explained by specific dynamical pathways (see section 4.2 above) which impact onto tropospheric circulation up to several months following an ENSO event, e.g., the connection of ENSO with the positive phase of the tropospheric PNA pattern [e.g., Lin et al., 2014].

Direct effects of warm and cool phases of ENSO on IASI O₃ records are further represented in Figure 12 which shows the tropical distributions of IASI O₃ tropospheric columns during the peak activity for ENSO during the period of IASI observations in November–December 2015 and the cool phase for La Niña in November–December 2010, in comparison with a reference period characterized by no ENSO

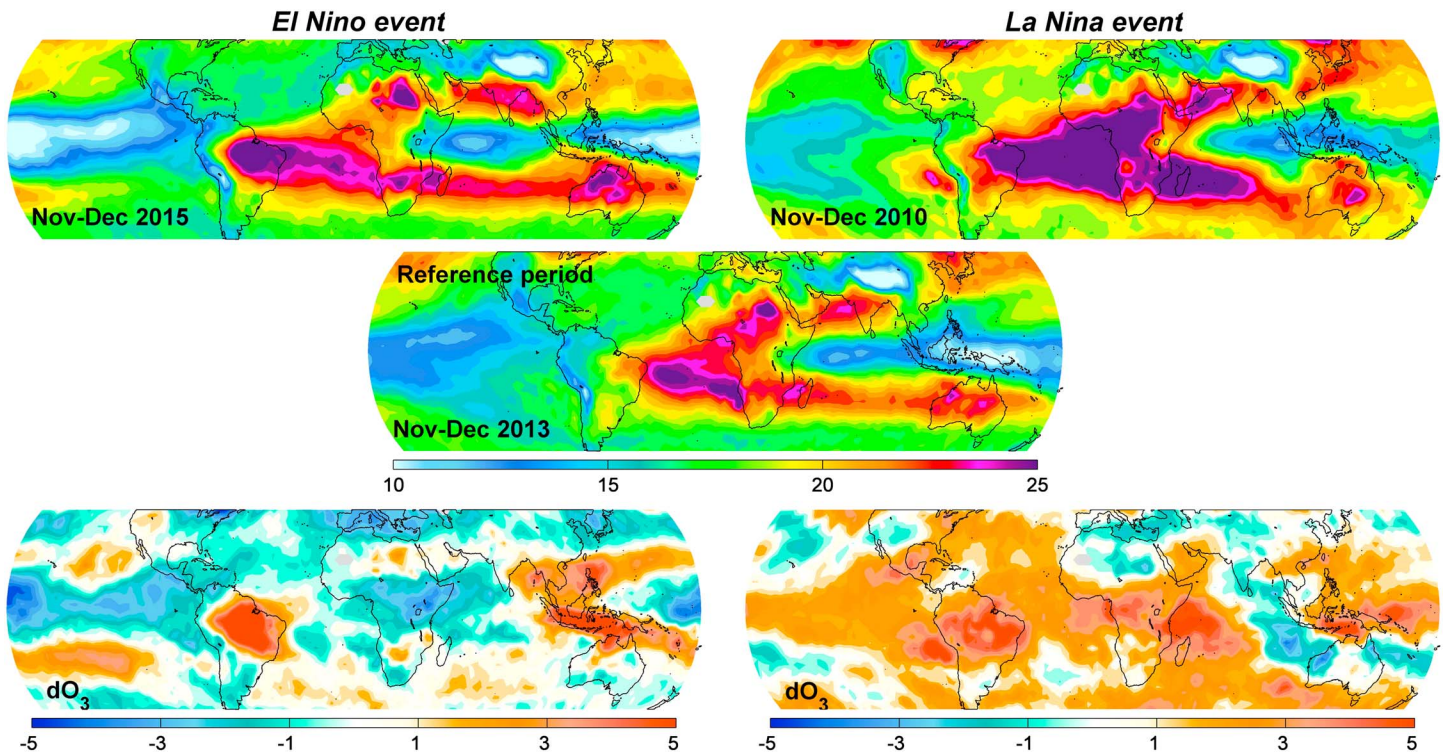


Figure 12. Global distribution of IASI O₃ tropospheric columns during (top row) strong El Niño (November–December 2015) and medium La Niña (November–December 2010) episodes compared with a (middle) reference period (November–December 2013) and (bottom row) their differences (dO_3) (in Dobson unit).

activity (November–December 2013). Interestingly, we see from the differences (dO_3 in DU) that the warm phase shows (Figure 12, bottom left) a clear resemblance with that of the ENSO regression coefficients in Figure 8 (ENSO panel), especially with respect to the strong tropical–extratropical and west–east gradients related to the dynamical and the chemical effects of El Niño, respectively. The difference distributions for the cool La Niña conditions highlight opposite impacts which result from a reduction in fires in Indonesia/Northern Australia and an increase in South America [e.g., Valks *et al.*, 2014]. These difference distributions further confirm the representativeness of the adjusted ENSO index in the regression models.

5. Summary and Conclusions

In this study, we have examined the capability of the IASI sounder to provide meaningful chemical and dynamical information on tropospheric O₃ variations. Our analyses used the first 8 years of IASI daily measurements (January 2008 to March 2016). We have demonstrated first the ability of IASI for capturing large-scale variability of tropospheric ozone independently from the upper layers: specific patterns of deseasonalized anomalies in the MLT compared to the upper layers (UTLS, MLS, and US) have been identified with low correlations between them. The deseasonalized distributions were hypothesized to be mostly controlled by the El Niño–Southern Oscillation effect with the highest anomalies found over the tropical Pacific, especially during the DJF and MAM periods (~25%). To verify this, the tropospheric ozone response to the main geophysical O₃ drivers has been explored for the first time for IASI on the global scale by applying a multivariate regression model (annual and seasonal formulations), including chemical and dynamical proxies, on gridded mean tropospheric ozone time series. The performance of the two models has been investigated in terms of residual errors and chi-squared statistic. The results demonstrate that both regression models reproduce well the daily IASI observations with very low relative differences (<1%) and no specific bias. The regression models were also shown to explain most of the IASI variations over the globe, especially in the tropical band during the DJF and MAM periods, which corresponds to the area and the period of greatest anomalies, where the model contribution reaches 90%. Using the chi-squared statistics, we further

demonstrated that the seasonal model outperforms the annual one for ~50% of the gridded mean time series, mainly located in the tropics and also in the N.H. According to these results, the explanatory variables were analyzed from the adjustment of the two models. The regression coefficients for the annual harmonic terms present clear hemispheric patterns which explain ~50% of the IASI variations, reproduce the winter-spring annual maxima in both hemispheres, and, therefore, reflect the photochemical O₃ production. The variations on shorter time scales (6, 4, and 3 month) were found to modulate the annual variation in the tropics, especially over the Indian/western Pacific Oceans.

The analysis of the non-seasonal parameters has shown that the solar flux, AAO, PV, and GEO proxies are generally minor components (relative contribution < 10%), while NAO, QBO, and ENSO show clear strong contributions with marked regional differences in the regression coefficients. A clear NAO influence is captured with regions of positive and negative O₃ responses which are coincident with the variation of the pressure dipole between the Icelandic/Arctic and the subtropical Atlantic regions. The NAO effect is shown to explain ~20% of the interannual variability of ozone in the north Atlantic region. A clear band-like structure in the tropics with a strong equatorial/extra-equatorial gradient was highlighted from the adjustment of the QBO proxies with a contribution of up to 45% to the O₃ variations. That specific meridional distribution along with an additional smoother gradient from the tropics to the poles further supports the detection of the QBO signature in IASI O₃. The regression results also showed a strong influence of the El Niño–Southern Oscillation on the tropospheric O₃ variations in the tropics with typical tropical-extratropical and west-east gradients resulting from a combination of dynamical and chemical effects. This was particularly observed during the DJF period, which coincides with the highest detected IASI anomalies and the largest ENSO activity. ENSO was modeled as the main contributor to the tropospheric O₃ variations in the tropical band (contribution reaching ~55%). A midlatitude ozone response to ENSO was also found, but it is not as strong as in the tropics. It was further investigated by including time-lagged ENSO proxies in the models for parameterizing time lags relation between ENSO and O₃. This improved the quality fits, especially in the equatorial band and in the N.H, and highlighted, for the MAM and the JJA periods, a 4-month lag over the middle and high latitudes of the N.H. This possible 4-month lag, which is observed for the first time from satellite measurements, constitutes an important value of this study. It was also further detected by analyzing ENSO signatures during strong to moderate El Niño episodes in both tropical and extratropical regions.

This finding opens perspectives for potentially using the observed 4-month ENSO lag in the response of O₃ to ENSO as a constraint on CCMs that include the ENSO-related O₃ variations as a forcing mechanism. Examining the ability of the CCMs to determine the response of tropospheric O₃ to ENSO into the middle and high latitudes could constitute a useful tool for better understanding and predicting future O₃ changes.

Further investigations on the O₃ anomalies, on the O₃ regressors dependencies, and on the O₃ trends derived from accurate multiple linear regression with predictor functions will be achievable in the future using the long-term homogeneous records obtained by merging O₃ measurements from the three successive IASI instruments on MetOp-A (2006), MetOp-B (2012), and MetOp-C (2018) and by IASI successor on EPS-SG after 2021 [Clerbaux and Crevoisier, 2013; Crevoisier et al., 2014].

Acknowledgments

IASI has been developed and built under the responsibility of the Centre National d'Etudes Spatiales (CNES, France). It is flown on board the MetOp satellites as part of the EUMETSAT Polar System. The IASI L1 data are received through the EUMETCast near real-time data distribution service. Ozone data used in this paper are freely available upon request to the corresponding author. We acknowledge support from the O₃-CCI project funded by ESA, from the O3M-SAF project funded by EUMETSAT, and from the EU-FP7 PANDA project (<http://www.marcopolopanda.eu/>). The research in Belgium was also funded by the Belgian State Federal Office for Scientific, Technical, and Cultural Affairs and the European Space Agency (ESA Prodex IASI Flow and O₃MSAF).

References

- Anton, M., et al. (2011), Validation of the Metop-A total ozone data from GOME-2 and IASI using reference ground-based measurements at the Iberian peninsula, *Remote Sens. Environ.*, *115*, 1380–1386.
- August, T., D. Klaes, P. Schlüssel, T. Hultberg, M. Crapeau, A. Arriaga, A. O'Carroll, D. Coppens, R. Munro, and X. Calbet (2012), IASI on Metop-A: Operational level 2 retrievals after five years in orbit, *J. Quant. Spectros. Radiat. Transfer*, *114*(11), 1340–1371.
- Austin, J., L. L. Hood, and B. E. Soukharev (2007), Solar cycle variations of stratospheric ozone and temperature in simulations of a coupled chemistry-climate model, *Atmos. Chem. Phys.*, *7*, 1693–1706.
- Baldwin, M. P., et al. (2001), The quasi-biennial oscillation, *Rev. Geophys.*, *39*, 179–230, doi:10.1029/1999RG000073.
- Bönisch, H., A. Engel, T. Birner, P. Hoor, D. W. Tarasick, and E. A. Ray (2011), On the structural changes in the Brewer-Dobson circulation after 2000, *Atmos. Chem. Phys.*, *11*, 3937–3948, doi:10.5194/acp-11-3937-2011.
- Boynard, A., et al. (2016), Seven years of IASI ozone retrievals from FORLI: Validation with independent total column and vertical profile measurements, *Atmos. Meas. Tech. Discuss.*, doi:10.5194/amt-2016-11.
- Bronnimann, S., J. Luterbacher, J. Staehelin, T. M. Svendby, G. Hansen, and T. Svenøe (2004), Extreme climate of the global troposphere and stratosphere in 1940–42 related to El Niño, *Nature*, *431*, 971–974.
- Butler, A. H., M. Polvani, and C. Deser (2014), Separating the stratospheric and tropospheric pathways of El Niño–Southern Oscillation teleconnections, *Environ. Res. Lett.*, *9*(2), 024014, doi:10.1088/1748-9326/9/2/024014.
- Chandler, R. E., and E. M. Scott (2011), *Statistical Methods for Trend Detection and Analysis in the Environmental Sciences, Statistics in Practice*, John Wiley, Chichester, U. K.

- Chandra, S., J. R. Ziemke, W. Min, and W. G. Read (1998), Effects of 1997–1998 El Niño on tropospheric ozone and water vapor, *Geophys. Res. Lett.*, **25**, 3867–3870, doi:10.1029/98GL02695.
- Chandra, S., J. R. Ziemke, P. K. Bhartia, and R. V. Martin (2002), Tropical tropospheric ozone: Implications for dynamics and biomass burning, *J. Geophys. Res.*, **107**(D14), 4188, doi:10.1029/2001JD000447.
- Chandra, S., J. R. Ziemke, M. R. Schoeberl, L. Froidevaux, W. G. Read, P. F. Levelt, and P. K. Bhartia (2007), Effects of the 2004 El Niño on tropospheric ozone and water vapor, *Geophys. Res. Lett.*, **34**, L06802, doi:10.1029/2006GL028779.
- Chipperfield, M. P., J. S. Kinnery, and J. Zawodny (1994), A two-dimensional model study of the QBO signal in SAGE II NO₂ and O₃, *Geophys. Res. Lett.*, **21**, 589–592, doi:10.1029/94GL00211.
- Christensen, R. (2015), *Analysis of Variance, Design, and Regression: Linear Modeling for Unbalanced Data*, 2nd ed., CRC Press, Boca Raton, Fla.
- Clarisse, L., Y. R'Honi, P.-F. Coheur, D. Hurtmans, and C. Clerbaux (2011), Thermal infrared nadir observations of 24 atmospheric gases, *Geophys. Res. Lett.*, **38**, L10802, doi:10.1029/2011GL047271.
- Clerbaux, C., and C. Crevoisier (2013), New directions: Infrared remote sensing of the troposphere from satellite: Less, but better, *Atmos. Environ.*, **72**, 24–26.
- Clerbaux, C., et al. (2009), Monitoring of atmospheric composition using the thermal infrared IASI/MetOp sounder, *Atmos. Chem. Phys.*, **9**, 6041–6054.
- Cooper, O., D. Parrish, A. Stohl, M. Trainer, P. Nédélec, V. Thouret, J.-P. Cammas, S. Oltmans, B. Johnson, and D. Tarasick (2010), Increasing springtime ozone mixing ratios in the free troposphere over western North America, *Nature*, **463**, 344–348, doi:10.1038/nature08708.
- Creilson, J. K., J. Fishman, and A. E. Wozniak (2003), Intercontinental transport of tropospheric ozone: A study of its seasonal variability across the North Atlantic utilizing tropospheric ozone residuals and its relationship to the North Atlantic Oscillation, *Atmos. Chem. Phys.*, **3**, 2053–2066.
- Crevoisier, C., et al. (2014), Towards IASI-New Generation (IASI-NG): Impact of improved spectral resolution and radiometric noise on the retrieval of thermodynamic, chemistry and climate variables, *Atmos. Meas. Tech.*, **7**, 4367–4385.
- Dufour, G., M. Eremenko, J. Orphal, and J.-M. Flaud (2010), IASI observations of seasonal and day-to-day variations of tropospheric ozone over three highly populated areas of China: Beijing, Shanghai, and Hong Kong, *Atmos. Chem. Phys.*, **10**, 3787–3801.
- Dufour, G., M. Eremenko, A. Griesfeller, B. Barret, E. LeFlochmoen, C. Clerbaux, J. Hadji-Lazaro, P.-F. Coheur, and D. Hurtmans (2012), Validation of three different scientific ozone products retrieved from IASI spectra using ozonesondes, *Atmos. Meas. Tech.*, **5**, 611–630.
- Ebojje, F., J. P. Burrows, C. Gebhardt, A. Ladstätter-Weißmayer, C. von Savigny, A. Rozanov, M. Weber, and H. Bovensmann (2016), Global tropospheric ozone variations from 2003 to 2011 as seen by SCIAMACHY, *Atmos. Chem. Phys.*, **16**, 417–436, doi:10.5194/acp-16-417-2016.
- Eremenko, M., G. Dufour, G. Foret, C. Keim, J. Orphal, M. Beekmann, G. Bergametti, and J.-M. Flaud (2008), Tropospheric ozone distributions over Europe during the heat wave in July 2007 observed from infrared nadir spectra recorded by IASI, *Geophys. Res. Lett.*, **35**, L18805, doi:10.1029/2008GL034803.
- Fiore, A., F. Dentener, O. Wild, C. Cuvelier, M. Schultz, P. Hess, C. Textor, M. Schulz, R. Doherty, and L. Horowitz (2009), Long-range transport, tropospheric ozone, pollution, *J. Geophys. Res.*, **114**, D04301, doi:10.1029/2008JD010816.
- Fishman, J., C. E. Watson, J. C. Larsen, and J. A. Logan (1990), Distribution of tropospheric ozone determined from satellite data, *J. Geophys. Res.*, **95**(D2), 3599–3617, doi:10.1029/JD095iD04p03599.
- Fishman, J., J. K. Creilson, A. E. Wozniak, and P. J. Crutzen (2005), The interannual variability of stratospheric and tropospheric ozone determined from satellite measurements, *J. Geophys. Res.*, **110**, D20306, doi:10.1029/2005JD005868.
- Flury, T., D. L. Wu, and W. G. Read (2013), Variability in the speed of the Brewer–Dobson circulation as observed by Aura/MLS, *Atmos. Chem. Phys.*, **13**, 4563–4575.
- Franzke, C., S. B. Feldstein, and S. Lee (2011), Synoptic analysis of the Pacific–North American teleconnection pattern, *Q. J. R. Meteorol. Soc.*, **137**, 329–346.
- Frossard, L., H. E. Rieder, M. Ribatet, J. Staehelin, J. A. Maeder, S. Di Rocco, A. C. Davison, and T. Pete (2013), On the relationship between total ozone and atmospheric dynamics and chemistry at mid-latitudes—Part 1: Statistical models and spatial fingerprints of atmospheric dynamics and chemistry, *Atmos. Chem. Phys.*, **13**, 147–164, doi:10.5194/acp-13-147-2013.
- Fusco, A. C., and J. A. Logan (2003), Analysis of 1970–1995 trends in tropospheric ozone at Northern Hemisphere midlatitudes with the GEOSCHEM model, *J. Geophys. Res.*, **108**(D15), 4449, doi:10.1029/2002JD002742.
- Gazeaux, J., et al. (2012), Intercomparison of polar ozone profiles by IASI/Metop sounder with 2010 concordiasi ozonesonde observations, *Atmos. Meas. Tech.*, **5**, 7923–7944.
- Hess, P. G., and R. Zbinden (2013), Stratospheric impact on tropospheric ozone variability and trends: 1990–200, *Atmos. Chem. Phys.*, **13**, 649–674.
- Heue, K.-P., M. Coldewey-Egbers, A. Delcloo, C. Lerot, D. Loyola, P. Valks, and M. van Roozendael (2016), Trends of tropical tropospheric ozone from twenty years of European satellite measurements and perspectives for Sentinel-5 Precursor, *Atmos. Meas. Tech. Discuss.*, doi:10.5194/amt-2016-139.
- Hilton, F., et al. (2012), Hyperspectral Earth Observation from IASI: Five Years of Accomplishments, *Bull. Am. Meteorol. Soc.*, **93**(3), 347–370.
- Hood, L. L. (1997), The solar cycle variation of total ozone: Dynamical forcing in the lower stratosphere, *J. Geophys. Res.*, **102**, 1355–1370, doi:10.1029/96JD00210.
- Hood, L. L., and B. E. Soukharev (2003), Quasi-decadal variability of the tropical lower stratosphere: The role of extratropical wave forcing, *J. Atmos. Sci.*, **60**, 2389–2403.
- Hudman, R. C., et al. (2004), Ozone production in transpacific Asian pollution plumes and implications for ozone air quality in California, *J. Geophys. Res.*, **109**, D23510, doi:10.1029/2004JD004974.
- Huesmann, A. S., and M. H. Hitchman (2001), The stratospheric quasi-biennial oscillation in the NCEP reanalyses: Climatological structures, *J. Geophys. Res.*, **106**, 11,859–11,874, doi:10.1029/2001JD900031.
- Hurrell, J. W. (1995), Decadal trends in the North Atlantic Oscillation regional temperatures and precipitation, *Science*, **269**, 676–679.
- Hurtmans, D., P. Coheur, C. Wespes, L. Clarisse, O. Scharf, C. Clerbaux, J. Hadji-Lazaro, M. George, and S. Turquety (2012), FORLI radiative transfer and retrieval code for IASI, *J. Quant. Spectros. Radiat. Transfer*, **113**, 1391–1408.
- Intergovernmental Panel on Climate Change (2007), Summary for Policymakers, in *Climate Change 2007: The Physical Science Basis, Contribution of Working Group I to the Fourth Assessment Report of the Intergovernmental Panel on Climate Change*, edited by S. Solomon et al., Cambridge Univ. Press, Cambridge, U. K., and New York.
- Jones, A., et al. (2009), Evolution of stratospheric ozone and water vapour time series studied with satellite measurements, *Atmos. Chem. Phys.*, **9**, 6055–6075.
- Knibbe, J. S., R. J. van der A, and A. T. J. de Laat (2014), Spatial regression analysis on 32 years of total column ozone data, *Atmos. Chem. Phys.*, **14**, 8461–8482.
- Kodera, K. and Y. Kuroda (2002), Dynamical response to the solar cycle, *J. Geophys. Res.*, **107**(D24), 4749, doi:10.1029/2002JD002224.

- Koumoutsaris, S., I. Bey, S. Generoso, and V. Thouret (2008), Influence of El Niño–Southern oscillation on the interannual variability of tropospheric ozone in the northern midlatitudes, *J. Geophys. Res.*, *113*, D19301, doi:10.1029/2007JD009753.
- Langford, A. O. (1999), Stratosphere-troposphere exchange at the subtropical jet: Contribution to the tropospheric ozone budget at mid-latitudes, *Geophys. Res. Lett.*, *26*, 2449–2452, doi:10.1029/1999GL900556.
- Langford, A. O., T. J. O’Leary, C. D. Masters, K. C. Aikin, and M. H. Proffitt (1998), Modulation of middle and upper tropospheric ozone at northern midlatitudes by the El Niño/Southern Oscillation, *Geophys. Res. Lett.*, *25*(14), 2667–2670, doi:10.1029/98GL01909.
- Li, Q., et al. (2005), Convective outflow of South Asian pollution: A global CTM simulation compared with EOS MLS observations, *Geophys. Res. Lett.*, *32*, L14826, doi:10.1029/2005GL022762.
- Lin, M., L. W. Horowitz, S. J. Oltmans, A. M. Fiore, and S. Fan (2014), Tropospheric ozone trends at Mauna Loa Observatory tied to decadal climate variability, *Nat. Geosci.*, *7*, 136–143.
- Logan, J. A. (1985), Tropospheric ozone: Seasonal behaviour, trends, and anthropogenic influence, *J. Geophys. Res.*, *90*(D6), 10,463–10,482, doi:10.1029/JD090iD06p10463.
- Logan, J. A. (1999), An analysis of ozonesonde data for the troposphere: Recommendations for testing 3-D models and development of a gridded climatology for tropospheric ozone, *J. Geophys. Res.*, *104*, 16,115–16,149, doi:10.1029/1998JD100096.
- Logan, J. A., et al. (2012), Changes in ozone over Europe: Analysis of ozone measurements from sondes, regular aircraft (MOZAIC) and alpine surface sites, *J. Geophys. Res.*, *117*, D09301, doi:10.1029/2011JD016952.
- Logan, J. A., D. B. A. Jones, I. A. Megretskaya, S. J. Oltmans, B. J. Johnson, H. V. omel, W. J. Randel, W. Kimani, and F. J. Schmidlin (2003), Quasi-biennial oscillation in tropical ozone as revealed by ozonesonde and satellite data, *J. Geophys. Res.*, *108*(D8), 4244, doi:10.1029/2002JD002170.
- Mäder, J. A., J. Staehelin, D. Brunner, W. A. Stahel, I. Wohltmann, and T. Peter (2007), Statistical modelling of total ozone: Selection of appropriate explanatory variables, *J. Geophys. Res.*, *112*, D11108, doi:10.1029/2006JD007694.
- Mäder, J. A., J. Staehelin, T. Peter, D. Brunner, H. E. Rieder, and W. A. Stahel (2010), Evidence for the effectiveness of the Montreal Protocol to protect the ozone layer, *Atmos. Chem. Phys.*, *10*, 12,161–12,171.
- McCormack, J. P., D. E. Siskind, and L. L. Hood (2007), Solar-QBO interaction and its impact on stratospheric ozone in a zonally averaged photochemical transport model of the middle atmosphere, *J. Geophys. Res.*, *112*, D16109, doi:10.1029/2006JD008369.
- McPeters, R. D., G. J. Labow, and J. A. Logan (2007), Ozone climatological profiles for satellite retrieval algorithms, *J. Geophys. Res.*, *112*, D05308, doi:10.1029/2005JD006823.
- Neu, J. L., T. Flury, G. L. Manney, M. L. Santee, N. J. Livesey, and J. Worden (2014), Tropospheric ozone variations governed by changes in stratospheric circulation, *Nat. Geosci.*, *7*, 340–344, doi:10.1038/ngeo2138.
- Newman, P. A., E. R. Nash, and J. Rosenfield (2001), What controls the temperature of the Arctic stratosphere during the spring?, *J. Geophys. Res.*, *106*, 19,999–20,010, doi:10.1029/2000JD000061.
- Oetjen, H., et al. (2014), Extending the satellite data record of tropospheric ozone profiles from Aura-TES to MetOp-IASI, *Atmos. Meas. Tech.*, *7*, 4223–4236, doi:10.5194/amt-7-4223-2014.
- Olsen, M. A., K. Wargan, and S. Pawson (2016), Tropospheric column ozone response to ENSO in GEOS-5 assimilation of OMI and MLS ozone data, *Atmos. Chem. Phys.*, *16*, 7091–7103, doi:10.5194/acp-16-7091-2016.
- Oltmans, S., et al. (2006), Long-term changes in tropospheric ozone, *Atmos. Environ.*, *40*, 3156–3173.
- Oman, L. D., A. R. Douglass, J. R. Ziemke, J. M. Rodriguez, D. W. Waugh, and J. E. Nielsen (2013), The ozone response to ENSO in Aura satellite measurements and a chemistry–climate simulation, *J. Geophys. Res. Atmos.*, *118*, 965–976, doi:10.1029/2012JD018546.
- Parrington, M., et al. (2012), The influence of boreal biomass burning emissions on the distribution of tropospheric ozone over north America and the north Atlantic during 2010, *Atmos. Chem. Phys.*, *12*, 2077–2098, doi:10.5194/acp-12-2077-2012.
- Parrish, D. D., et al. (2012), Long-term changes in lower tropospheric baseline ozone concentrations at northern mid-latitudes, *Atmos. Chem. Phys.*, *12*, 11,485–11,504.
- Pausata, F. S. R., L. Pozzoli, E. Vignati, and F. J. Dentener (2012), North Atlantic Oscillation and tropospheric ozone variability in Europe: Model analysis and measurements intercomparison, *Atmos. Chem. Phys. Discuss.*, *12*, 3131–3167, doi:10.5194/acpd-12-3131-2012.
- Pommier, M., et al. (2012), Analysis of IASI tropospheric O₃ data over the arctic during POLARCAT campaigns in 2008, *Atmos. Chem. Phys.*, *12*, 7371–7389, doi:10.5194/acp-12-7371-2012.
- Randel, W. J., and A. M. Thompson (2011), Inter-annual variability and trends in tropical ozone derived from SAGE II satellite data and SHADOZ ozonesondes, *J. Geophys. Res.*, *116*, D07303, doi:10.1029/2010JD015195.
- Randel, W. J., and F. Wu (1996), Isolation of the ozone QBO in SAGE II data by singular-value decomposition, *J. Atmos. Sci.*, *53*, 2546–2559.
- Randel, W. J., and F. Wu (2007), A stratospheric ozone profile data set for 1979–2005: Variability, trends, and comparisons with column ozone data, *J. Geophys. Res.*, *112*, D06313, doi:10.1029/2006JD007339.
- Randel, W. J., F. Wu, and R. Stolarski (2002), Changes in column ozone correlated with the stratospheric EP flux, *J. Meteorol. Soc. Jpn.*, *80*, 849–862.
- Rieder, H. E., L. Frossard, M. Ribatet, J. Staehelin, J. A. Maeder, S. Di Rocco, A. C. Davison, T. Peter, P. Weihs, and F. Holawe (2013), On the relationship between total ozone and atmospheric dynamics and chemistry at mid-latitudes—Part 2: The effects of the El Niño/Southern Oscillation, volcanic eruptions and contributions of atmospheric dynamics and chemistry to long-term total ozone changes, *Atmos. Chem. Phys.*, *13*, 165–179.
- Rodgers, C. D. (2000), *Inverse Methods for Atmospheric Sounding: Theory and Practice*, Ser. Atmos. Oceanic Planet. Phys., vol. 2, World Sci., Hackensack, N. J.
- Safieddine, S., C. Clerbaux, M. George, J. Hadji-Lazaro, D. Hurtmans, P.-F. Coheur, C. Wespes, D. Loyola, P. Valks, and N. Hao (2013), Tropospheric ozone and nitrogen dioxide measurements in urban and rural regions as seen by IASI and GOME-2, *J. Geophys. Res. Atmos.*, *118*, 10,555–10,566, doi:10.1002/jgrd.50669.
- Safieddine, S., et al. (2014), Summertime tropospheric ozone assessment over the Mediterranean region using the thermal infrared IASI/MetOp sounder and the WRF-Chem model, *Atmos. Chem. Phys.*, *14*, 10,119–10,131, doi:10.5194/acp-14-10119-2014.
- Salby, M. L., and P. F. Callaghan (2006), Influence of the Brewer–Dobson circulation on stratosphere-troposphere exchange, *J. Geophys. Res.*, *111*, D21106, doi:10.1029/2006JD007051.
- Scannell, C., D. Hurtmans, A. Boynard, J. Hadji-Lazaro, M. George, A. Delcloo, A. Tuinder, P. F. Coheur, and C. Clerbaux (2012), Antarctic ozone hole as observed by IASI/MetOp for 2008–2010, *Atmos. Meas. Tech.*, *5*, 123–139.
- Soukharev, B. E., and L. L. Hood (2006), Solar cycle variation of stratospheric ozone: Multiple regression analysis of long-term satellite data sets and comparisons with models, *J. Geophys. Res.*, *111*, D20314, doi:10.1029/2006JD007107.
- Stohl, A., S. Eckhardt, C. Forster, P. James, and N. Spichtinger (2002), On the pathways and timescales of intercontinental air pollution transport, *J. Geophys. Res.*, *107*(D23), 4684, doi:10.1029/2001JD001396.

- Steinbrecht, W., H. Claude, and P. Winkler (2004), Enhanced upper stratospheric ozone: Sign of recovery or solar cycle effect?, *J. Geophys. Res.*, *109*, D02308, doi:10.1029/2003JD004284.
- Tarasick, D. W., V. E. Fioletov, D. I. Wardle, J. B. Kerr, and J. Davies (2005), Changes in the vertical distribution of ozone over Canada from ozonesondes: 1980–2001, *J. Geophys. Res.*, *110*, D02304, doi:10.1029/2004JD004643.
- Terao, Y., J. A. Logan, A. R. Douglass, and R. S. Stolarski (2008), Contribution of stratospheric ozone to the interannual variability of tropospheric ozone in the northern extratropics, *J. Geophys. Res.*, *113*, D18309, doi:10.1029/2008JD009854.
- Thompson, D. W. J., and J. M. Wallace (2000), Annular modes in the extratropical circulation. Part I: Month-to-month variability, *J. Clim.*, *13*, 1000–1016.
- Thouret, V., J.-P. Cammas, B. Sauvage, G. Athier, R. Zbinden, R. P. Nédélec, P. Simon, and F. Karcher (2006), Tropopause referenced ozone climatology and inter-annual variability (1994–2003) from the MOZAIK programme, *Atmos. Chem. Phys.*, *6*, 1033–1051, doi:10.5194/acp-6-1033-2006.
- Tian, W., M. P. Chipperfield, L. J. Gray, and J. M. Zawodny (2006), Quasi-biennial oscillation and tracer distributions in a coupled chemistry-climate model, *J. Geophys. Res.*, *111*, D20301, doi:10.1029/2005JD006871.
- Valks, P., N. Hao, S. Gimeno Garcia, D. Loyola, M. Dameris, P. Jöckel, and A. Delcloo (2014), Tropical tropospheric ozone column retrieval for GOME-2, *Atmos. Meas. Tech.*, *7*, 2513–2530, doi:10.5194/amt-7-2513-2014.
- Vestreng, V., L. Ntziachristos, A. Semb, S. Reis, I. S. A. Isaksen, and L. Tarraso (2009), Evolution of NO_x emissions in Europe with focus on road transport control measures, *Atmos. Chem. Phys.*, *9*, 1503–1520, doi:10.5194/acp-9-1503-2009.
- Voulgarakis, A., P. Hadjinicolaou, and J. A. Pyle (2011), Increases in global tropospheric ozone following an El Niño event: Examining stratospheric ozone variability as a potential driver, *Atmos. Sci. Lett.*, *12*, 228–232, doi:10.1002/asl.318.
- Wang, Y., and D. J. Jacob (1998), Anthropogenic forcing on tropospheric ozone and OH since preindustrial times, *J. Geophys. Res.*, *103*, 31,123–31,135, doi:10.1029/1998JD100004.
- Wespes, C., et al. (2012), Analysis of ozone and nitric acid in spring and summer arctic pollution using aircraft, ground-based, satellite observations and MOZART-4 model: Source attribution and partitioning, *Atmos. Chem. Phys.*, *12*, 237–259.
- Wespes, C., D. Hurtmans, L. K. Emmons, S. Safieddine, C. Clerbaux, D. P. Edwards, and P.-F. Coheur (2016), Ozone variability in the troposphere and the stratosphere from the first six years of IASI observations (2008–2013), *Atmos. Chem. Phys.*, *16*, 5721–5743.
- Wilks, D. S. (2011), *Statistical Methods in the Atmospheric Sciences*, 3rd ed., Academic Press, Amsterdam.
- Wilson, R. C., Z. L. Fleming, P. S. Monks, G. Clain, S. Henne, I. B. Kononov, S. Szopa, and L. Menut (2012), Have primary emission reduction measures reduced ozone across Europe? An analysis of European rural background ozone trends 1996–2005, *Atmos. Chem. Phys.*, *12*, 437–454, doi:10.5194/acp-12-437-2012.
- Witte, J. C., M. R. Schoeberl, A. R. Douglass, and A. M. Thompson (2008), The Quasi-biennial Oscillation and annual variations in tropical ozone from SHADOZ and HALOE, *Atmos. Chem. Phys.*, *8*, 3929–3936.
- Wolter, K., and M. S. Timlin (2011), El Niño/Southern Oscillation behaviour since 1871 as diagnosed in an extended multivariate ENSO index (MEI_{ext}), *Int. J. Climatol.*, *31*, 1074–1087.
- Worden, J., et al. (2013), El Niño, the 2006 Indonesian peat fires, and the distribution of atmospheric methane, *Geophys. Res. Lett.*, *40*, 4938–4943, doi:10.1002/grl.50937.
- Zbinden, R. M., J.-P. Cammas, V. Thouret, P. Nédélec, F. Karcher, and P. Simon (2006), Mid-latitude tropospheric ozone columns from the MOZAIK program: Climatology and interannual variability, *Atmos. Chem. Phys.*, *6*, 1053–1073, doi:10.5194/acp-6-1053-2006.
- Zeng, G., and J. A. Pyle (2005), Influence of El Niño Southern Oscillation on stratosphere/troposphere exchange and the global tropospheric ozone budget, *Geophys. Res. Lett.*, *32*, L01814, doi:10.1029/2004GL021353.
- Ziemke, J. R., and S. Chandra (2003), La Niña and El Niño-induced variabilities of ozone in the tropical lower atmosphere during 1970–2001, *Geophys. Res. Lett.*, *30*(3), 1142, doi:10.1029/2002GL016387.
- Ziemke, J. R., S. Chandra, L. D. Oman, and P. K. Bhartia (2010), A new ENSO index derived from satellite measurements of column ozone, *Atmos. Chem. Phys.*, *10*, 3711–3721, doi:10.5194/acp-10-3711-2010.
- Ziemke, J. R., et al. (2014), Assessment and applications of NASA ozone data products derived from Aura OMI/MLS satellite measurements in context of the GMI chemical transport model, *J. Geophys. Res. Atmos.*, *119*, 5671–5699, doi:10.1002/2013JD020914.
- Ziemke, J. R., A. R. Douglass, L. D. Oman, S. E. Strahan, and B. N. Duncan (2015), Tropospheric ozone variability in the tropics from ENSO to MJO and shorter timescales, *Atmos. Chem. Phys.*, *15*, 8037–8049.